Astrocyte GluN2C NMDA receptors control basal synaptic strengths of hippocampal CA1 pyramidal neurons in the *stratum radiatum*

Peter H. Chipman[1,5], Alejandra Pazo Fernandez[1,4], Chi Chung Alan Fung[2,4], Angelo Tedoldi[1], Atsushi Kawai[1], Sunita Ghimire Gautam[1,6], Mizuki Kurosawa[1], Manabu Abe[3], Kenji Sakimura[3], Tomoki Fukai[2] and Yukiko Goda[1,*]

[1]RIKEN Center for Brain Science, Wako-shi, Saitama 351-0198, Japan
[2]Neural Coding and Brain Computing Unit, Okinawa Institute of Science and Technology, Onna-son, Kunigami-gun, Okinawa, 904-0495, Japan
[3]Department of Animal Model Development, Brain Research Institute, Niigata University, Niigata, 951-8585, Japan
[4]These authors contributed equally.
[5]Present address: Department of Biochemistry and Biophysics, University of California, San Francisco, San Francisco, CA 94158, USA
[6]Present address: Shikhar Biotech Pvt. Ltd, Lalitpur, Nepal
*Correspondence: yukiko.goda@riken.jp

1   **Summary**

2   Experience-dependent plasticity is a key feature of brain synapses for which neuronal N-Methyl-

3   D-Aspartate receptors (NMDARs) play a major role, from developmental circuit refinement to

4   learning and memory. Astrocytes also express NMDARs although their exact function has

5   remained controversial. Here we identify a circuit function for GluN2C NMDAR, a subtype highly

6   expressed in astrocytes, in layer-specific tuning of synaptic strengths in mouse hippocampal CA1

7   pyramidal neurons. Interfering with astrocyte NMDAR or GluN2C NMDAR activity reduces the

8   range of presynaptic strength distribution specifically in the *stratum radiatum* inputs without an

9   appreciable change in the mean presynaptic strength. Mathematical modeling shows that

10   narrowing of the width of presynaptic release probability distribution compromises the

11   expression of long-term synaptic plasticity. Our findings suggest a novel feedback signaling

12   system that uses astrocyte GluN2C NMDARs to adjust basal synaptic weight distribution of

13   Schaffer collateral inputs, which in turn impacts computations performed by the CA1 pyramidal

14   neuron.

15

16

17

18   **Key words**

19   Basal synaptic strength; Hippocampus; Astrocytes; NMDA receptors; GluN2C;

20   Layer-specificity; Synaptic plasticity; *Stratum radiatum*

Introduction

Plasticity is a fundamental feature of neuronal connections in the brain, where experience-dependent changes in synaptic strengths over different time scales are crucial for a variety of processes ranging from neural circuit development, circuit computations to learning and memory (Feldman and Brecht, 2005; Bliss and Collingridge, 1993; Abbott and Regehr, 2004; Collingridge et al., 2010; Nicoll, 2017). Deciphering how neurons dynamically express different forms of synaptic plasticity while ensuring the optimal performance of the circuit remains a key challenge (Vitureira and Goda, 2013; Turrigiano, 2017; Nicoll, 2017; Brunel, 2016). In particular, the distribution of synaptic strengths is thought to reflect the capacity or the state of information storage of neural circuits (Barbour et al., 2007; Buzsáki and Mizuseki, 2014; Bromer et al., 2018). A better understanding of the cellular mechanisms that regulate synaptic strength distribution could therefore provide novel insights into the basis for the effective execution of circuit operations (Barbour et al., 2007).

The N-methyl-D-aspartate receptors (NMDARs) are a major ionotropic glutamate receptor type mediating excitatory synaptic transmission (Paoletti et al., 2013; Sanz-Clemente et al., 2013; Hansen et al., 2018). NMDARs are heteromeric assemblies consisting of four subunits, and seven NMDAR subunit genes have been identified that fall into three subfamilies: *Grin1* encoding the obligatory GluN1 subunit, four *Grin2* genes encoding GluN2A-D, and two *Grin3* genes encoding GluN3A-B (Paoletti et al., 2013; Hansen et al., 2018). The differing subunit compositions confer NMDARs with distinct biophysical and pharmacological properties and contribute to their diverse biological activities. NMDARs are expressed throughout the central nervous system (CNS) and are crucial for normal brain function and plasticity. In particular, NMDARs that are typically composed of two GluN1 and two GluN2 subunits and are present postsynaptically have been extensively studied for their role in memory mechanisms (Paoletti et al., 2013; Sanz-Clemente et al., 2013; Nicoll 2017). NMDARs are also involved in pathological conditions such as epilepsy, ischemia, and traumatic brain injury (Hansen et al., 2017). In stark contrast to the multifaceted functions of neuronal NMDARs, very little is known of NMDAR functions in glial cells in the CNS. Amongst the better characterized glial NMDARs, NMDARs in oligodendrocytes play a role in axonal energy metabolism (Saab et al., 2016) and exacerbate pathological conditions (Karadottir et al., 2005). In astrocytes, NMDARs have been long thought to be absent except following ischemia *in vivo* or under anoxia *in vitro* that promote their aberrant expression (Krebs et al., 2003; Gottlieb and Matute, 1997). Nevertheless, there are reports of GluN2C mRNA expression in astrocytes in the adult brain (Watanabe et al., 1993; Karavanova et al., 2007; Ravikrishnan et al., 2018), and several studies provide physiological evidence in support of astrocyte NMDAR expression under non-pathological conditions (Schipke et al., 2001; Serrano et al., 2008; Lalo et al., 2006; Letellier et al., 2016). The precise function for astrocyte NMDARs, however, has

57 remained a matter of debate (e.g. Kirchhoff, 2017), and the role for astrocyte GluN2C has not yet
58 been identified.

59   Astrocytes regulate a diverse set of essential brain activities, from neurovascular coupling,
60 metabolic support, and ionic homeostasis (e.g. Attwell et al., 2010; Giaume et al., 2010; Simard and
61 Nedergaard, 2004) to synaptic connectivity and function (e.g. Araque et al., 2014; Clarke and
62 Barres, 2013). Recent studies have highlighted a role for astrocytes in the bidirectional control of
63 basal synaptic transmission (Panatier et al., 2011; Perea and Araque; 2007; DiCastro et al., 2011;
64 Martin-Fernandez et al., 2017; Schwarz et al., 2017), which likely involves signaling via their
65 perisynaptic processes (Bindocci et al., 2017; Bazargani and Attwell, 2016). Moreover, mounting
66 evidence suggests that astrocytes are not only capable of either simply potentiating (Panatier et
67 al., 2011; Perea and Araque, 2007; Jourdain et al., 2007) or depressing synaptic transmission
68 (Martín et al., 2015; Pascual et al., 2005), but a single astrocyte, which contacts tens of thousands
69 of synapses, can concurrently mediate bi-directional synapse regulation at separate synaptic
70 contact sites (Schwarz et al., 2017; Covelo and Araque, 2018). Astrocytes likely regulate neural
71 circuit functions at multiple levels, as suggested by observations of both local and global astrocyte
72 signaling that are triggered in a synapse, neuron, or circuit-specific manner (Martín-Fernandez et
73 al., 2017; Martín et al., 2015; Chai et al., 2017; Deemyad et al., 2018; Dallérac et al., 2018; Santello
74 et al., 2019). However, despite these advances, the basic mechanisms by which astrocytes detect
75 and adjust synaptic transmission and the extent of their impact on local synaptic circuit activity
76 are not fully understood.

77   Astrocytes express a plethora of neurotransmitter receptors and membrane transporters
78 that are thought to modulate synaptic transmission (Araque et al., 2014; Bazargani and Attwell,
79 2016), including perisynaptic astrocyte glutamate transporters that influence the magnitude and
80 kinetics of postsynaptic glutamate receptor activation and membrane depolarization (Pannasch
81 et al., 2014; Murphy-Royal et al, 2015) and astrocyte metabotropic glutamate receptors (mGluRs)
82 whose activation promote gliotransmitter release to provide feedback control of synaptic
83 transmission (Panatier et al., 2011; Schwarz et al., 2017; Covelo and Araque, 2018; Araque et al.,
84 2014; Bazargani and Attwell, 2016). Given the often shared expression of neurotransmitter
85 receptors and transporters between astrocytes and neurons, an important challenge is to
86 decipher the synaptic activity-dependent functions of astrocyte receptors and transporters
87 independently of the functions of their neuronal counterparts. Notably, many of the prior studies
88 have focused on pathological brain states (Krebs et al., 2003; Gottlieb and Matute, 1997) or used
89 young brain tissue (e.g. Panatier et al., 2011) or culture preparations (e.g. Schwarz et al., 2017) in
90 which the expression pattern of the astrocyte receptors and channels differ substantially from the
91 adult brain in basal conditions (Sun et al., 2013; also see Boisvert et al., 2018). Consequently, the

92   cellular basis and the network consequences of astrocyte-synapse interactions mediated by the

93   astrocyte receptors and channels in the healthy adult brain remain to be clarified.

94   In a previous study, we identified a role for astrocyte signaling in regulating synaptic

95   strength heterogeneity in hippocampal neurons, which involved astrocyte NMDARs (Letellier et

96   al., 2016). Heterogeneity was assessed by comparing the presynaptic strengths of two

97   independent inputs to pyramidal neurons, which was estimated by the paired-pulse ratio (PPR)

98   of excitatory postsynaptic current (EPSC) amplitudes, a parameter inversely related to

99   presynaptic release probability (Dobrunz and Stevens, 1997). Although basal PPRs were

100   uncorrelated between the two inputs, surprisingly, inhibiting astrocyte NMDARs promoted the

101   correlation of PPRs. This indicated that astrocyte NMDARs contributed to enhancing the

102   differences in basal presynaptic strengths represented by the two different inputs (Letellier et al.,

103   2016). Such pair-wise comparison of PPRs, however, is limited to providing an indirect measure

104   of variability, and it remains unclear how astrocyte NMDARs control the overall shape of the PPR

105   distribution. Furthermore, the crucial roles for neuronal NMDARs in regulating synaptic

106   transmission and plasticity have confounded the interpretation of astrocyte NMDAR functions,

107   which still remain enigmatic (Kirchhoff, 2017). Here, we further investigated astrocyte NMDAR-

108   dependent regulation of synaptic strength in hippocampal CA1 pyramidal neurons in adult mice,

109   focusing on the mode of regulation of presynaptic strength distribution, the NMDAR type

110   responsible, and probing the potential layer specific regulation in area CA1. Our findings identify

111   a role for astrocyte GluN2C NMDARs in maintaining broad presynaptic strength diversity

112   specifically in the *stratum radiatum* (SR) by enhancing both strong and weak synapses.

113   Mathematical modeling suggests that presynaptic strength diversity strongly influences the

114   expression of long-term synaptic plasticity, which in turn, is important for network stability and

115   learning and memory (Malenka and Bear, 2004; Collingridge et al., 2010; Royer and Paré, 2003;

116   Zenke and Gerstner, 2017). Our findings suggest astrocyte GluN2C NMDARs as a key player in

117   linking the regulation of synaptic strength distribution to the expression of synaptic plasticity that

118   promotes optimal circuit performance.

119

120   **Results**

121   *NMDAR-dependent regulation of PPR variability in hippocampal CA1 pyramidal neurons*

122   In order to characterize the properties of astrocyte NMDAR-dependent modulation of synaptic

123   strength, here we devised a simplified assay using a single stimulating electrode to monitor PPR

124   variability of Schaffer collateral synapses. Hippocampal slices were prepared from adult mouse

125   brain (P60-120), and EPSCs to a pairwise stimulation (50 ms inter-stimulus interval) of Schaffer

126   collateral axons were recorded in CA1 pyramidal neurons (Figure 1A; Figure S1). MK-801 (1 mM)

127   was infused into the postsynaptic cell via the patch pipette, and after 10-15 min but prior to

128   starting the experiment, Schaffer collaterals were stimulated at 0.1 Hz for at least 45 times to pre-
129   block synaptic NMDARs. This resulted in over 92% inhibition of synaptic NMDAR currents
130   (Bender et al 2006) (Figure S1; see methods). Upon confirming the block of postsynaptic NMDARs,
131   the baseline EPSC recordings were taken; subsequently NMDAR inhibitors were bath applied to
132   test their effects on PPR variance. Under the block of postsynaptic NMDARs, any effects of NMDAR
133   inhibitors, if observed, would be expected to reflect the influence of NMDARs present either in
134   astrocytes or the presynaptic neurons. Notably, in mature brains which we used for our
135   experiments, the contribution of presynaptic NMDARs in general had been suggested be minimal
136   (Shih et al., 2013). Upon bath applying MK801 (50 μM) or AP5 (50 μM), the population variance
137   (δ^2) of PPRs was reduced without a significant change in the mean ($\bar{x}$) (Figure 1B-D; MK801 δ^2
138   p=.016, $\bar{x}$ p=.856; AP5, δ^2 p=.047; $\bar{x}$ p=.162). This overall decrease in PPR variance, when
139   examined at the level of individual inputs, was associated with a change in PPR (ΔPPR) that was
140   negatively correlated to the baseline PPR: PPR of some inputs increased while others decreased
141   by the NMDAR antagonist application (Figure 1E-G). Furthermore, consistent with a lack of change
142   in the mean PPR upon blocking NMDARs, a linear fit to the data intercepted the x-axis near the
143   baseline mean PPR (x-axis intercept: MK801 = 1.97; AP5 = 1.95).

144   We also tested for the contribution of GluN2B NMDAR and also of mGluR5 in maintaining
145   PPR variance. Bath applying Ro25-6981 (10 μM), a GluN2B-specific NMDAR antagonist (Fischer
146   et al., 1997), and MPEP (25 μM), an mGluR5-specific antagonist (Gasparini et al., 1999), had little
147   effect on PPR variance (Figure S2A-C; Ro256981 p=.362, MPEP p=.349). MPEP, however,
148   significantly increased the mean PPR (Figure S2C; p=.033), which is consistent with a reported
149   role for mGluR5 in presynaptic strength regulation (Panatier et al 2011).

150   We next examined whether the changes in PPR elicited by the extracellularly applied
151   NMDAR inhibitors accompanied changes in the EPSC amplitude and the coefficient of variation
152   (CV) of EPSC amplitude, the latter as an additional measure of the change in presynaptic release
153   probability (Malinow and Tsien, 1990; Larkman et al, 1992). On average, bath applied MK801 did
154   not substantially alter the amplitude of the first EPSC to the pair of stimuli relative to control slices,
155   despite a small tendency for an increase with a time delay (Figure 1I; p= .657). MK801 also had
156   little effect on CV^{-2} of EPSC amplitudes (Figure S3B; p= .991), although the responses of individual
157   inputs to MK801, albeit small in magnitude, were positively correlated to CV^{-2} (Figure S3D;
158   Pearson's r = .420, p = .026) and negatively correlated to PPR (Figure S3H; Pearson's r = -.474, p
159   = .011). These data are consistent with the possibility that the observed reduction in PPR diversity
160   by MK801 application is associated with normalization of presynaptic release probability.

161   In contrast to MK801, AP5 significantly increased EPSC amplitudes within 10 min of
162   application (Figure 1J; p = .026), and the increase in CV^{-2} (Figure S3B; AP5 p = .003) suggested that
163   the change in EPSC amplitude involved a presynaptic change. Notably, Ro25-6981 that had no

6

164   effect on PPR variance, did produce a significant increase in CV^{-2} (Figure S2H; CV^{-2} p = .002), and

165   produced a small but non-significant increase in EPSC amplitudes (Figure S2E; EPSC p = .261),

166   which was consistent with the observed increase in PPR (above). None of the NMDAR antagonists

167   caused substantial changes in the amplitude or frequency of spontaneous EPSCs (sEPSCs) or

168   evoked EPSC waveforms (Figure S4).

169   We next sought to confirm the NMDAR-dependent modulation of presynaptic strength

170   diversity as described in our previous study by comparing PPRs across two independent Schafer

171   collateral inputs that converge onto a target CA1 pyramidal neuron (Letellier et al., 2016), and to

172   observe the time course of PPR population variance change by NMDAR antagonists. In this

173   method, the absolute difference of PPRs between the two inputs (PPR disparity) is taken as a

174   proxy for presynaptic strength variability, with lower PPR disparity indicating lower PPR

175   variability and vice versa (Figure S5A,B). Consistent with our analysis thus far, bath application of

176   MK801 and AP5 reduced PPR disparity (Figure S5D,E; MK801 p = .001, AP5 p=.004), while Ro25-

177   6981 and MPEP did not (Figure S5G,H; Ro25-6981 p = .670, MPEP p = .263).

178   Collectively, these findings support the idea NMDARs play a role in bi-directionally

179   regulating presynaptic strengths to broaden the variability of PPR. Moreover, such an involvement

180   of NMDARs in presynaptic regulation is distinct from the presynaptic regulation by mGluR5 that

181   potentiates synaptic strength across a synapse population.

182

183   *Astrocyte NMDARs mediate the effects of NMDAR antagonists on PPR diversity*

184   To test the extent to which bath applied NMDAR antagonists affected synaptic transmission by

185   targeting astrocyte NMDARs, we knocked down in astrocytes, the *GRIN1* gene that encodes GluN1,

186   a requisite subunit for the cell surface expression of NMDARs (Fukaya et al., 2003; Abe et al.,

187   2004). AAV carrying either mCherry-tagged nlsCre (Cre) or a control nls-mCherry lacking Cre

188   (ΔCre) under the GFAP104 promoter was injected bilaterally into the dorsal hippocampus of adult

189   *GRIN1* floxed mice (Figure 2A)(Letellier et al., 2016). We used low titer AAVs (~0.4-4E10 genome

190   copies/injection) to avoid potential reactive astrocytosis, and although the extent was modest, we

191   obtained a highly specific mCherry expression in astrocytes throughout the area CA1 with little

192   expression in neurons (Figure 2B: Cre, 41.1 ± 2.4% of GFAP+ve cells [n = 3529], 0.3 ± 0.1% of

193   NeuN+ve cells [n = 1150] from 5 mice; ΔCre, 40.7 ± 1.9% of GFAP+ve cells [n = 3309], 0.5 ± 0.1%

194   of NeuN+ve cells [n = 1217] from 5 mice). The efficacy of GluN1 knock-down in astrocytes was

195   assessed electrophysiologically by patch-clamping astrocytes and monitoring slow depolarizing

196   responses elicited by puff applying NMDA and glycine (1mM each) (Figure S6)(Letellier et al.,

197   2016). Astrocytes that expressed Cre as identified by the mCherry fluorescence in *stratum*

198   *radiatum* (SR) where Schafer collateral synapses were present, showed depolarizing responses to

199   NMDA-glycine puff that were significantly decreased compared to ΔCre controls (Figure S6A; p =

7

200   0.006). Given that mCherry-positive astrocytes were present throughout the CA1, we also
201   monitored NMDA-glycine puff responses in astrocytes in *stratum oriens* (SO) and *stratum*
202   *lacunosum moleculare* (SLM). In contrast to mCherry-positive astrocytes in SR, mCherry-labelled
203   astrocytes in SO or SLM showed depolarizing responses to NMDA-glycine puff that were not
204   different between Cre and control ΔCre slices (Figure S6B-C; SO p = .247; SLM p = .268), despite
205   the fact that viral transduction efficiencies were comparable amongst astrocytes across the three
206   layers (SR: Cre 39.8 ± 2.4%, ΔCre 40.2 ± 2.0%; SO: Cre 44.8 ± 3.0%, ΔCre 39.3 ± 5.9%; SLM: Cre
207   39.1 ± 4.9%, ΔCre 40.0 ± 4.0%). The input resistance of patched astrocytes was not altered by Cre
208   expression in any layer (Figure S6D). Notably NMDA-glycine responses in SLM were substantially
209   smaller than those in SR or SO (p = 0.001, one way ANOVA, Bonferroni post-hoc tests).
210   Nevertheless, AP5 bath application blocked NMDA-glycine puff-induced depolarizing responses
211   in astrocytes in all three layers. This observation suggests that NMDARs are broadly expressed
212   across hippocampal CA1 astrocytes. Moreover, the differential sensitivity of the slow depolarizing
213   responses to astrocyte GluN1 knock-down between layers supports the possibility that the
214   cumulative actions of signaling downstream to NMDAR activation including the contribution of
215   voltage-gated conductances (Serrano et al., 2008; Letellier et al., 2016; Shih et al., 2013) could be
216   heterogeneous across layers. We will return to this layer-specific differences later.

217   Having detected GluN1-dependent functional NMDAR activity in SR CA1 astrocytes, we
218   next asked whether the GluN1 knock-down also affected synaptic transmission of Schaffer
219   collateral synapses similarly to the bath applied NMDAR antagonists. Baseline PPR showed a
220   significantly reduced PPR variance in Cre-infected slices compared to control slices without a
221   change in the mean PPR (Figure 2C,D; δ^2 p = .033; $\bar{x}$ p = .725). Analysis of the relative PPR from
222   two independent Schaffer collateral inputs also revealed lower PPR disparity in Cre injected slices
223   compared to control slices (Figure S7A; p = .009). These observations are consistent with a
224   reduced PPR variance upon compromising astrocyte NMDAR signaling as observed with bath
225   applied NMDAR inhibitors. The amplitude and frequency of spontaneous EPSCs and the waveform
226   of evoked EPSCs were unaltered by astrocyte-specific GluN1 knock-down (Figure S7B,C).

227   We next determined whether astrocyte GluN1 knock-down could occlude the effects of
228   bath applied AP5 on PPR variance, by recording from postsynaptic CA1 neurons infused with
229   MK801 in ΔCre and Cre-infected slices. Similar to naïve slices, in ΔCre control slices, AP5
230   decreased the population variance of PPRs by strengthening some synapses and weakening
231   others (Figure 2E; ΔCre +AP5 p = .017). In addition, AP5 caused also a variable increase in EPSC
232   amplitudes (Figure 2G; AP5 p = .005) that occurred without a concomitant change in the
233   amplitude or the frequency of spontaneous EPSCs (Figure S7D,E). In Cre slices, however, the
234   decrease in PPR variance by AP5 was strongly attenuated, despite the modest extent of virus
235   infection in Cre slices (Figure 2F; Cre +AP5 p = .789). The analysis of PPR disparity across two

236   inputs also showed substantially decreased inhibitory effect of AP5 in Cre slices relative to
237   controls (Figure S7H,I; ΔCre +AP5 p = .013, Cre +AP5 p =.315). Curiously, the small increase in
238   EPSC amplitudes observed upon applying AP5 was also attenuated in Cre slices (Figure 2H). This
239   suggests that although the effect of NMDAR antagonists on PPR diversity and EPSC amplitudes are
240   likely to target distinct compartments – presynaptic and postsynaptic – both mechanisms may
241   involve astrocyte NMDARs. Together, these observations indicate that astrocyte NMDARs are the
242   major mediators of the synaptic effects of acutely blocking NMDARs in our experimental
243   conditions, and further support the view that astrocyte NMDARs help maintain the broad
244   variability of presynaptic strengths across a synapse population.

245

246   *Modelling of release probability variability reveals its impact on synaptic plasticity*
247   In order to gain an insight into the physiological role for the broad release probability distribution,
248   we sought to assess the impact of reducing the presynaptic strength variability on a synaptic
249   learning rule by constructing a mathematical model. We first modelled release probability
250   variations based on log-normal distributions (Buzsáki and Mizuseki, 2014; Branco and Staras,
251   2009; Murthy et al., 1997) for a range of peak release probability distributions (U_{max}) that
252   represented the control condition and when the variance was reduced to mimic conditions of
253   astrocyte NMDAR blockade, termed "control" and "NMDAR blocked", respectively (Figure 3A; see
254   Methods). The optimal parameters for the log-normal distributions were obtained from the best
255   fit to a modified synaptic facilitation model based on Tsodyks et al. (1998) using the experimental
256   data in which the peak EPSC amplitudes to repetitive stimulation of the Schaffer collaterals at 20
257   Hz were monitored under identical conditions to the PPR experiments (Figure S8A; see Methods).
258   Next, we used the BCM learning rule (Bienenstock et al., 1982) to investigate potential
259   implications of altering the variance of release probability on long-term synaptic plasticity. In the
260   BCM learning rule, the synaptic weight undergoes changes according to the excitatory
261   postsynaptic current and the presynaptic neurotransmitter release, in which the magnitude and
262   the type of long-term plasticity can be controlled by a set of parameters (see Methods). In
263   simulations, we explored the effect caused by decreasing the variance of the release probability
264   on both long-term potentiation (LTP) and long-term depression (LTD). Figure 3B illustrates an
265   example experiment for U_{max} = 0.1, where traces of the synaptic weight function $w(t)$ for LTP and
266   LTD are two conditions that differ only with respect to the release probability variance of the
267   presynaptic neuron. Application of 100 presynaptic spikes with 50-ms inter-spike intervals
268   triggered a rapid change in synaptic weight during the stimulation that was stably maintained
269   after the stimulation for both LTP and LTD (Figure 3B). Although the efficacy of both LTP and LTD
270   are reduced in the condition of less variable release probability mimicking the NMDAR-block
271   situation, the effect is larger for LTP.

9

272   We next sought to test whether the qualitative result of the simulation is preserved over
273   a range of LTP and LTD (i.e. for a series of parameter α; see Methods). To this end, the difference
274   of synaptic weight change induced by stimulation between conditions of broad (control) vs.
275   narrow (NMDAR block) release probability variability was considered as a function of a range of
276   the absolute change in synaptic weight $w(t)$ under control release probability conditions for both
277   LTP and LTD (Figure 3C, solid lines). In the numerical exploration, we found that LTD was always
278   smaller if the pre-synaptic neuron had less variable release probability. In contrast, the sensitivity
279   of LTP to release probability variance depended on the magnitude of potentiation, in which the
280   adverse effect of the narrowing of release probability distribution in compromising synaptic
281   plasticity was increasingly pronounced with a larger degree of potentiation. The robustness of the
282   observed sensitivity of LTP and LTD to the differences in release probability variance was further
283   tested by changing the peak release probability U_{max} under the same conditions (U_{max} = 0.10, 0.15,
284   0.20). The overall pattern of the decrease in the efficacy of LTP and LTD persisted upon narrowing
285   the release probability distribution. However, the reduction of LTD became less prominent when
286   U_{max} was increased (Figure 3C).

287   In order to determine whether the influence of release probability variance on the efficacy
288   of long-term plasticity could be observed in a different model, spike-timing dependent plasticity
289   (STDP) was simulated using synaptically connected two leaky integrate-and-fire (LIF) neurons
290   (see Methods). The presynaptic neuron received a spike train of 500 mA magnitude, A_1, while the
291   postsynaptic neuron received a spike train of variable magnitude A_2. Pairing 10 spikes at 20 Hz
292   with a time difference between spike trains of Δt resulted in LTP or LTD, with positive Δt values
293   producing LTP and negative Δt values resulting in LTD (Figure 3D(i)). Notably, conditions that
294   mimic decreased release probability variance seen in NMDAR-blocked experiments showed no
295   observable changes in LTD whereas LTP was compromised compared to control conditions
296   (Figure 3D(ii)), the latter effect on LTP being similar to the observations in the BCM-like model.

297   Finally, the impact of narrowing the release probability variance was explored under a
298   more general STDP scenario by examining synaptic weight changes elicited in a pair of neurons
299   receiving Poisson spike trains. Specifically, the synaptic weights obtained in response to the same
300   Poisson sequences in the control condition or the NMDAR-blocked condition for a number of
301   independent simulations at U_{max} of 0.10 showed that the efficacy of potentiation was consistently
302   smaller in the NMDAR-blocked condition (Figure 3E). Such an attenuating effect of the reduced
303   release probability variance on potentiation was observed also when the peak of release
304   probability distributions was shifted to larger values (U_{max} = 0.15 and 0.20; Figure S8C).

305   Altogether, the numerical simulation experiments demonstrate that a reduced variability
306   in presynaptic release probability can reshape the long-term synaptic plasticity dynamics. In the
307   BCM-like model, both LTP and LTD were reduced, and in the LIF-neuron-pair model, LTP was

10

308   reduced whereas LTD appeared largely unchanged. Collectively, LTP is likely to be compromised

309   across a synapse population when the distribution of release probability is narrowed, while the

310   effect on LTD could depend on the fine detail of the spike sequence.

311

312   *Hippocampal astrocytes express GluN2C NMDARs*

313   Our results thus far point to astrocyte NMDARs, and in particular, the involvement of the

314   obligatory subunit GluN1 in regulating the variability of presynaptic strengths. In order to obtain

315   direct molecular evidence for the expression of NMDAR in hippocampal astrocytes and to clarify

316   the relevant NMDAR subtype, we performed single cell RT-PCR to compare the expression of

317   GluN1, GluN2A, GluN2B and GluN2C mRNAs in CA1 astrocytes across SO, SR and SLM layers and

318   CA1 pyramidal neurons (Figure 4A). Acute hippocampal slices were prepared from adult mice as

319   used for electrophysiology experiments, and after labelling astrocytes with sulforhodamine101

320   (Nimmerjahn et al., 2004), RNA from single cells was extracted by patch-clamping. All putative

321   astrocytes had low input resistances (SR 11.20 ± 0.36 MΩ; SO 13.24 ± 0.43 MΩ; SLM 10.60 ± 0.33

322   MΩ; n = 39 cells from 9 mice sampled for each layer), lacked action potentials, and displayed linear

323   current-voltage relationships (Figure 4A,B). CA1 pyramidal neurons expressed high levels of

324   GluN1, GluN2A and GluN2B subunit mRNAs but expressed substantially low levels of GluN2C

325   mRNA. In contrast, astrocytes in all three layers showed robust expression of GluN2C mRNA.

326   Moreover, astrocytes showed minimal expression of GluN2A and GluN2B mRNAs, and the GluN1

327   mRNA expression in astrocytes was also substantially low compared to neurons (Figure 4C).

328   GluN2D mRNA in CA1 pyramidal neurons and astrocytes was also tested, and it was undetectable

329   in RNA extracted from patch clamping both cell types while the probe itself could detect GluN2D

330   mRNA in brain tissue extracts (data not shown). Inability to detect GluN2D mRNA in astrocytes is

331   consistent with previous reports of single cell RNA-seq analysis (Khakh Lab database; also see

332   Alsaad et al., 2019). We also examined the levels of expression of NMDAR subunits in CA3

333   pyramidal neurons, and the pattern of subunit expression mirrored the pattern observed for CA1

334   pyramidal neurons (data not shown).

335   The expression of GluN2C subunit protein in the hippocampus was confirmed by

336   immunoprecipitation of mouse hippocampal extracts followed by Western blotting, using an

337   antibody against the Cre recombinase that is not expressed in wild type mice, as a negative control

338   (Figure 4D). For characterizing the cellular expression pattern of GluN2C in the hippocampus, we

339   were unable to identify an antibody against GluN2C that was suitable for immunofluorescence

340   labelling experiments. Therefore, in order to visualize the cells that expressed GluN2C, we used a

341   GluN2C mutant mouse line carrying an insertion of a codon-improved Cre recombinase

342   immediately downstream of the translation initiation site in the *GRIN2C* gene (Miyazaki et al.,

343   2012). GluN2C-Cre mice were crossed with a Cre reporter line (Ai9: Madisen et al., 2010) that

11

344   expressed tdTomato upon Cre-mediated recombination. The hippocampus of the offspring

345   showed robust tdTomato fluorescence in astrocytes identified by GFAP labelling (81.6 ± 5.7% of

346   GFAP+ve cells; Figure 4E,F), which was consistent with the high expression level of GluN2C mRNA

347   in astrocytes (Figure 4C). Moreover, some interneurons in SR identified by the NeuN labeling also

348   expressed tdTomato (3.6 ± 1.6% of NeuN+ve cells in SR, Figure 4E,F), which was in agreement

349   with previous reports (Ravikrishnan et al., 2018; Gupta et al., 2016). Surprisingly, the pyramidal

350   cell layer also showed sporadic tdTomato-labelled neuronal cell bodies, although such cells

351   represented a limited proportion of pyramidal neurons (5.8 ± 1.0% of NeuN+ve cells in *stratum*

352   *pyramidale*, Figure 4E,F). The RT-PCR, biochemical and immunohistochemistry experiments

353   collectively provide evidence in support of GluN2C-containing NMDAR as a major NMDAR type

354   expressed in hippocampal CA1 astrocytes.

355

356   *Inhibition of GluN2C NMDARs reduces PPR variability in a manner sensitive to astrocyte GluN1*

357   *expression*

358   Given the prominent expression of GluN2C in astrocytes, we wondered if the regulation of PPR

359   could be attributed to GluN2C NMDARs. To test such a possibility, we examined whether

360   pharmacological inhibition of GluN2C NMDARs could mimic the effects of bath applied AP5 and

361   MK801 on PPR variance using QNZ46 (25 μM), an NMDAR antagonist specific for GluN2C/D

362   (Hansen and Traynelis, 2011). Similarly to MK801 and APV, QNZ46 reduced the population

363   variance of PPRs without altering the mean PPR (Figure 5A; δ^2 p=.008; $\bar{x}$ p=.312). Again we

364   observed the negative correlation between the change in PPR and the baseline PPR (Figure 5A,

365   bottom), with a linear fit to the data intercepting the x-axis near the baseline mean PPR (X

366   intercept = 2.07). Additionally, in experiments monitoring two independent Schaffer collateral

367   inputs, bath application of QNZ46 decreased the PPR disparity as found for AP5 and MK801

368   (Figure S5F; p = .005). These observations suggest that GluN2C/D-containing NMDARs contribute

369   to maintaining the broad PPR diversity. Given the lack of detectable expression of GluN2D in

370   hippocampal CA1 cells, it is likely that NMDARs containing GluN2C mediate the observed effects

371   of QNZ46 in modulating presynaptic strength to decrease the overall range of PPR variability.

372   When EPSC amplitudes were examined, QNZ46 bath application caused a significant

373   increase, reminiscent of the changes observed upon AP5 and MK801 application (Figure 5D; p =

374   .014). Moreover, similarly to AP5, QNZ46 significantly increased CV^{-2} of EPSC amplitudes (Figure

375   S3B; p = .009), which was suggestive of presynaptic alterations.

376   Next we asked whether QNZ46 acted on astrocyte NMDARs to control PPR variability. To

377   address this point, we again tested for occlusion using astrocyte GluN1 knock-down slices. QNZ46

378   was bath applied to Cre and ΔCre-infected slices while recording EPSCs from CA1 neurons infused

379   with MK801. In ΔCre control slices QNZ46 decreased the PPR variance (Figure 5B; p = .065) and

380   caused a variable increase in EPSC amplitudes (Figure 5E; p = .005) without a concomitant change

381   in the amplitude or the frequency of spontaneous EPSCs (Figure S7F). Crucially, as observed for

382   AP5, QNZ46 was no longer effective in producing a significant change in the PPR variance in Cre

383   slices (Figure 5C; p = .649). When PPR disparity across two inputs was monitored, QNZ46

384   decreased the PPR disparity in a manner that was sensitive to astrocyte GluN1 knock-down, which

385   also supported the involvement for GluN2C-NMDARs in regulating presynaptic strength diversity

386   (Figure S7J,K; ΔCre +QNZ46 p = .031; Cre +QNZ46 p = .126). Moreover, similarly to AP5, QNZ46-

387   dependent increase of EPSC amplitudes was attenuated also in Cre slices (Figure 5F).

388   Together, these observations indicate that GluN2C NMDARs expressed in astrocytes

389   function to maintain the broad variability of presynaptic strengths across a synapse population.

390   While GluN2C NMDARs also play a role in regulating EPSC amplitudes, this is likely to involve a

391   mechanism that is distinct from the presynaptic regulation but is engaged in parallel to target

392   postsynaptic processes.

393

394   *Layer-specific regulation of synaptic strength by astrocyte NMDARs*

395   Astrocytes are a highly heterogeneous cell type (Zhang and Barres, 2010; Khakh and Sofroniew,

396   2015) that influence synaptic transmission in a synapse- and circuit-specific manner (Martin-

397   Fernandez et al., 2017; Schwarz et al., 2017; Martin et al., 2015; Lanjakornsiripan et al., 2018). Our

398   RT-PCR analysis of NMDAR subtype expression showed relatively high expression of GluN2C

399   mRNA across SR, SO and SLM layers in CA1 astrocytes compared to CA1 pyramidal neurons.

400   Nevertheless, despite the relatively even expression of GluN2C across layers, our NMDA-glycine

401   puff application experiments CA1 astrocytes revealed layer-specific differences in the GluN1-

402   dependent component of the slow depolarizing responses triggered by the NMDA-glycine puff,

403   with SR astrocytes showing the highest sensitivity to the astrocyte GluN1 knock-down (Figure S6).

404   This raised the possibility that astrocyte NMDAR-dependent modulation of synaptic inputs to CA1

405   pyramidal neurons whose dendrites span across SR, SO and SLM, might also differ across layers.

406   To test such possibility of layer-specific regulation, we compared astrocyte NMDAR-

407   dependence of synaptic transmission in CA1 neurons across three layers in slices from astrocyte

408   GluN1 knock-down and control mice. In contrast to the specific decrease in the PPR variance

409   observed in Cre slices relative to ΔCre control slices for the SR input (Figure 2D), neither the PPR

410   variance nor its mean differed between Cre and ΔCre control slices for the SO and the SLM inputs

411   (Figure 6A-D; SO: δ^2 p = .303, $\bar{x}$ p = .402; SLM: δ^2 p = .624, $\bar{x}$ p = .161). We also examined the layer-

412   specificity of PPR diversity regulation using a pharmacological approach in slices from wild type

413   mice. The sensitivity of PPRs to bath applied NMDAR antagonists in CA1 pyramidal neurons

414   intracellularly perfused with MK801, was monitored in response to pairwise stimulation of SO

415   and SLM inputs as had been done for the SR input. Neither MK801 nor AP5 had any appreciable

13

416   effect on PPR variance in SO (Figure 6E,G: MK801, p = .107; AP5 p = .472) and SLM (Figure 6I,K:

417   MK801, p = .920; AP5, p = .741). MK801 modestly increased EPSC amplitudes at some inputs in

418   SO (Figure 6F: p = .783) but it had no effect in SLM (Figure 6J: p = .915). Moreover, AP5 did not

419   potentiate EPSC amplitudes as observed for the SR input, but instead it significantly depressed

420   EPSC amplitudes in SO (Figure 6H: p = .028) while it caused no appreciable change in SLM (Figure

421   6L: p = .317). Collectively, these results suggest that regulation of PPR diversity by astrocyte

422   NMDARs in CA1 pyramidal neurons is specific to the SR inputs.

423   As a further test of the layer specificity of astrocyte NMDAR-dependent regulation of PPR

424   variability, we assessed PPR disparity by performing two independent pathway analysis in each

425   layer in response to bath applied NMDAR antagonists. Again, in contrast to SR input (Figure S5D,

426   E), neither MK801 nor AP5 depressed the PPR disparity of the SO and the SLM inputs (Figure S9).

427   These observations are consistent with the role for astrocyte NMDARs, and particularly GluN2C

428   NMDARs, for maintaining the diversity of PPR specifically of SR inputs to CA1 pyramidal neurons.

429

430   **Discussion**

431   Broad heterogeneity in the efficacy of synaptic transmission is a fundamental feature of small

432   glutamatergic synapses in the mammalian brain (Dobrunz and Stevens, 1997; Atwood and

433   Karunanithi, 2002; Branco and Staras, 2009). A variety of presynaptic parameters contribute to

434   the observed variability, such as the abundance, subtype, and location of presynaptic calcium

435   channels (Thalhammer et al., 2017; Brenowitz and Regehr, 2007; Eltes et al., 2017), their

436   positioning with respect to the synaptic vesicles, the active zone size and the number of docked

437   vesicles, the state of vesicle fusion machinery (Park and Tsien, 2012; Marra et al., 2012; Fulterer

438   et al., 2018; Glebov et al., 2017; Holderith et al., 2012), as well as the coupling to neuromodulatory

439   signals (Burke et al., 2018), and the synapse's recent history of synaptic plasticity. These

440   determinants of presynaptic release efficacy are influenced by target-specific signals (Éltes et al.,

441   2017; Branco et al., 2008; Reyes et al., 1998; Markram et al., 1998) and are further subject to

442   activity-dependent modulation (Thalhammer et al., 2017; Goda and Stevens, 1998; Burke et al.,

443   2018). Although the basis for presynaptic release probability regulation at individual synapses

444   have been intensively studied, whether and how basal release probability variability is collectively

445   controlled across a synapse population is poorly understood, despite its implications in

446   information processing and memory storage (Barbour et al., 2007; Buzsáki and Mizuseki, 2014;

447   Bromer et al., 2018; Rotman and Klyachko, 2013). Our study highlights the novel contribution of

448   astrocyte GluN2C NMDAR signaling in broadening the range of basal release efficacy of Schaffer

449   collateral synapses by effectively maintaining strong synapses stronger and weaker synapses

450   weaker without an overt effect on the mean synaptic strength.

14

451   The present study took advantage of paired-pulse response, a short-term plasticity
452   inversely related to presynaptic release probability as a measure of presynaptic efficacy (Dobrunz
453   and Stevens, 1997), which in some experiments was further corroborated by the correlated
454   changes in CV^{-2} (Malinow and Tsien, 1990; Larkman et al., 1992). This study extends the concept
455   of NMDAR-mediated glial control of PPR (Letellier et al 2016) to include populations of synapses
456   within defined hippocampal subregions in the healthy adult mouse brain. Sampling a small
457   number of synapses by a relatively weak stimulation intensity (i.e. mean EPSC amplitude of ~60
458   ± 6 pA to Schaffer collateral stimulation in control condition) consistently revealed a component
459   of PPR distribution that was bi-directionally regulated by astrocyte NMDARs. Notably, such
460   modulation could be masked when sampling a large synapse population that yields stable
461   ensemble responses (Lines et al., 2017). Altogether, results from (i) pharmacological experiments
462   using subtype-specific NMDAR antagonists, which allowed monitoring the effects of NMDAR
463   inhibition in the same synapse population, (ii) the genetic interference specifically of astrocyte
464   NMDARs, and (iii) the cellular expression analysis of NMDAR subunits, collectively point to
465   GluN2C NMDAR as the major astrocyte receptor that regulates synaptic strength variability of
466   Schaffer collateral inputs.

467

468   *Functional significance of the broad distribution of presynaptic strengths*
469   What might be an advantage in maintaining a highly variable presynaptic efficacy across a synapse
470   population of a given input type? Our mathematical modeling and simulation data indicate that
471   the width of release probability distribution can bias the outcome of activity-dependent synaptic
472   plasticity. In the BCM-like model, a broad release probability distribution favors activity-
473   dependent synaptic depression, while for cases involving a large extent increase in synaptic
474   strength, increased release probability variance promotes potentiation. In a spiking neuron
475   model, the increased release probability variance also promoted LTP while the impact on LTD
476   may depend on the fine structure of the spikes. Notably, several studies have implicated astrocyte
477   signaling in LTD in hippocampal CA3 to CA1 synapses (Chen et al., 2013; Andrade-Talavera et al.,
478   2016; Navarrate et al., 2019; Pinto-Duarte et al., 2019), where spike timing-dependent LTD in
479   slices from young mice is sensitive to inhibitors of GluN2C/D, although the source of GluN2C/D
480   remains to be determined (Andrade-Talavera et al., 2016). Astrocyte GluN2C NMDAR-dependent
481   maintenance of variable basal presynaptic strengths of CA3 to CA1 synapses that we have
482   identified here could therefore be linked to astrocyte signaling that promotes LTP and LTD, which
483   in turn, are not only important for learning and memory but also for network stability
484   (Collingridge et al., 2010; Royer and Paré, 2003; Zenke and Gerstner, 2017). Curiously, this
485   GluN2C NMDAR-dependent broadening of the basal presynaptic efficacy in CA1 neurons is
486   confined to the SR inputs and not observed for SO or SLM inputs. This suggests that for dendritic

15

487 computations in CA1 pyramidal neurons, the broad variability of synaptic strengths at CA3-CA1

488 synapses is more crucial compared to the synaptic strength variability of basal or apical tuft

489 inputs. Mice deficient in GluN2C, while mostly normal in their behavior, show deficits in

490 acquisition of conditioned fear and working memory and changes in neuronal oscillations

491 (Hillman et al., 2011; Mao et al., 2020). Some population of interneurons express GluN2C, however

492 (Gupta et al., 2016; Ravikrishnan et al., 2018), and this confounds the interpretation of the

493 observed effects solely to deficits in astrocyte GluN2C. It would be of interest to determine in the

494 future whether there is a learning performance deficit in mice specifically deficient in astrocyte

495 GluN2C or GluN1 in the hippocampal CA1 subfield.

496   The mechanism by which astrocyte GluN2C NMDARs are coupled to the changes in

497 presynaptic efficacy remains to be clarified. The narrowing of the range of PPR suggest a bi-

498 directional modulation, in one possibility, that astrocyte NMDAR signaling could trigger the

499 release of two types of gliotransmitters with one potentiating and another depressing (Schwarz

500 et al., 2017; Covelo and Araque, 2018). Interestingly, astrocyte-mediated release of ATP, which is

501 converted to adenosine by extracellular ATPases, has been implicated in the bi-directional

502 modulation of presynaptic efficacy (Panatier et al., 2011; Pascual et al., 2005; Zhang et al., 2003;

503 Tan et al., 2017). The effects of adenosine depend in part on the presynaptic A_{2A} or A_1 receptors

504 that either enhance or suppress presynaptic function, respectively (Panatier et al., 2011; Tan et

505 al., 2017). Similarly, the relative abundance of A_{2A} or A_1 receptors at individual presynaptic

506 boutons could determine the polarity of presynaptic efficacy upon accumulation of extracellular

507 adenosine by the astrocyte GluN2C NMDAR activity. In another scenario, astrocyte GluN2C

508 receptors may influence the release of other gliotransmitters such as glutamate (Jourdain et al.,

509 2007) to target presynaptic or postsynaptic glutamate receptors and/or GluN2C receptor

510 signaling may influence astrocyte-mediated K^+ clearance to locally shape presynaptic action

511 potential waveforms (Cui et al., 2018) to in turn affect presynaptic efficacy.

512

513 *Astrocyte NMDAR subunit mRNAs and implications for layer-specific synapse modulation*

514 Previous transcriptome analysis of the major cell types in mouse cerebral cortex have suggested

515 that the GluN2C NMDAR subunit mRNA is one of the highly enriched transcripts in astrocytes,

516 whose level can be up to 70 fold of the level found in neurons (Zhang et al., 2014). Our single cell

517 RT-PCR analyses also show robust expression of GluN2C mRNA in astrocytes across the three CA1

518 layers in contrast to GluN2C mRNA expression in pyramidal neurons. Curiously, despite the high

519 expression of GluN2C mRNA in astrocytes, only low levels of GluN1 mRNA is detected in

520 astrocytes. This finding is unexpected given that GluN1 subunit is required for the surface

521 expression of functional NMDARs (Fukaya et al., 2003; Abe et al., 2004). Moreover, the observed

522 occlusion of QNZ46 effects on synaptic transmission by astrocyte-specific knock-down of GluN1

16

523 also support the presence of functional heteromeric GluN1/GluN2C NMDARs in astrocytes. The

524 whole-cell patch clamp method we used to collect RNAs is biased towards sampling of transcripts

525 that are abundant in the cell body. Given that astrocyte processes are numerous and thin, the

526 discordance between the detected GluN1 and GluN2C mRNA levels could be explained if the

527 mRNAs are differentially localized, with GluN1 mRNA being preferentially targeted to processes

528 compared to the cell body of astrocytes. Such a proposal is consistent with a recent study

529 reporting of GluN1 mRNA in astrocyte processes that is locally translated (Sakers et al., 2017). The

530 precise intracellular localization of NMDAR subunit mRNAs in astrocytes remains to be

531 determined.

532   The present study revealed synapse regulation by the astrocyte GluN2C NMDARs that is

533 confined to the SR input although GluN2C mRNA is expressed broadly across CA1 astrocyte layers.

534 Therefore, the layer-specificity of synaptic modulation could potentially arise from features of

535 GluN2C NMDAR assembly and trafficking and/or signaling that is unique to SR astrocytes over SO

536 and SLM astrocytes. In support of layer-specific differences in astrocyte NMDAR signaling, the

537 slow astrocyte membrane depolarization triggered by puff applied NMDA-glycine shows

538 significant dependence on astrocyte NMDAR only in SR and not in SO nor in SLM (Figure S6).

539 Additionally, differences in the properties of presynaptic inputs to CA1 pyramidal neuron

540 dendrites across layers (e.g. Schroeder et al., 2018) could also contribute to layer-specific synaptic

541 modulation by astrocyte GluN2C NMDARs.

542   The GluN2C subunit forms diheteromeric receptor complexes with the obligate GluN1

543 subunit and triheteromeric receptor complexes with GluN1 and GluN2A (Paoletti et al., 2013;

544 Hansen et al., 2018). The presence of GluN2C confers NMDAR properties that are distinct from

545 NMDARs containing GluN2A or GluN2B which are abundant in neurons. For example, GluN2C-

546 containing NMDARs show reduced channel open probability, increased glutamate sensitivity,

547 slow receptor deactivation, and a decreased sensitivity to Mg^{2+} block (Paoletti et al., 2013; Hansen

548 et al., 2018). Weak Mg^{2+} binding would enable open-pore blockers such as MK801, to nonetheless

549 rapidly exert their inhibitory action. Such reduced Mg^{2+} sensitivity of astrocyte NR2C NMDARs

550 could have contributed to the rapid effect observed for MK801 in normalizing presynaptic

551 strengths and reducing the PPR disparity. Moreover, the low EC_{50} of GluN2C-containing NMDAR

552 activation to glutamate (Hansen et al., 2018) suggests that they may be well suited for detecting

553 synaptic release events at perisynaptic astrocyte processes that can be at some distance from the

554 active zone. Several drugs that target NMDARs have been in clinical use, such as ketamine as an

555 anesthetic and treatment for depression (Krystal et al., 2019; Williams and Schatzberg, 2016) and

556 memantine for the treatment of moderate to severe dementia in Alzheimer's disease (Graham et

557 al., 2017). Under physiological conditions, GluN2C/GluN2D-containing NMDARs display up to 10-

558 fold higher sensitivity to ketamine and memantine in comparison to GluN2A/GluN2B-containing

559 NMDARs that are highly expressed in neurons (Kotermanski and Johnson, 2009; Hansen et al.,

560 2017). Therefore, although therapeutics targeting NMDARs to date have largely focused on

561 neuronal NMDARs, it would be crucial to consider also the consequences of interfering with

562 GluN2C NMDARs that are enriched in astrocytes, which is underscored by the increasing

563 recognition of the involvement of astrocytes in a variety of neurological disorders (Zuchero and

564 Barres, 2015; Chung et al., 2015).

565

566

567 **Materials and Methods**

568 *Slice preparation and whole cell recordings*

569 Mice (P60-120) were deeply anesthetized with isoflurane and transcardially perfused with ice-

570 cold cutting aCSF containing (in mM) 93 N-methyl D-glucamine, 2.5 KCl, 1.2 NaH_2PO_4, 30 $NaHCO_3$,

571 20 HEPES, 20 glucose, 5 Na ascorbate, 2 thiourea, 3 sodium pyruvate, 12 N-acetyl L-cysteine, 10

572 $MgSO_4$, 0.5 $CaCl_2$, pH adjusted to 7.4 with HCl and bubbled with 95% O_2 / 5% CO_2. Brains were

573 extracted and 350 μm transverse hippocampal slices were cut in ice-cold cutting aCSF on a Leica

574 VT1200 vibrating microtome. Slices were incubated for 12 min in cutting aCSF warmed to 34°C,

575 then placed in holding solution containing (in mM) 81.2 NaCl, 2.5 KCl, 1.2 NaH_2PO_4, 30 $NaHCO_3$,

576 20 HEPES, 20 D-glucose, 5 Na ascorbate, 2 thiourea, 3 sodium pyruvate, 12 N-acetyl L-cysteine, 2

577 $MgSO_4$, 2 $CaCl_2$, pH 7.4, bubbled with 95% O_2 / 5% CO_2 for up to 8 h. In some cases, slices were

578 incubated in 50 μM sulphorhodamine for 30 min at 34°C to identify astrocytes for RNA extraction.

579   Whole-cell patch clamp recordings were obtained from CA1 pyramidal neurons or

580 astrocytes using an Olympus BX51W1 microscope equipped with IR-DIC optics and a motorized

581 stage. Images were captured with a digital camera (Andor, iXion3) and imaged using MetaMorph

582 software (Molecular Devices). Voltage clamp and current clamp experiments were carried out

583 using Multiclamp 700B amplifiers (Molecular Devices) and up to four micromanipulators (SM5,

584 Luigs and Neumann). Patch pipettes (tip resistance 2-4 MΩ for neurons, 4-6 MΩ for astrocytes)

585 were pulled using a vertical 2-stage puller (PC-10 Narishige). Slices were constantly perfused with

586 recording aCSF containing (in mM) 119 NaCl, 2.5 KCl, 1.3 NaH_2PO_4, 26 $NaHCO_3$, 1 $MgCl_2$, 2 $CaCl_2$,

587 20 D-glucose and 0.5 Na ascorbate pH 7.4, bubbled with 95% O_2 / 5% CO_2 and maintained at 32-

588 34°C using an in-line heater (Harvard Instruments). Picrotoxin (100 μM) was added to the

589 recording aCSF to block $GABA_A$-receptors and isolate glutamatergic synaptic transmission.

590 Internal pipette solution contained (in mM) 130 $CsMeSO_3$, 8 NaCl, 4 Mg-ATP, 0.3 Na-GTP, 0.5

591 EGTA, 10 HEPES, pH 7.3, 290-295 mOsm for neuron recordings, and 130 K gluconate, 10 HEPES,

592 4 $MgCl_2$, 4 Na_2-ATP, 0.4 Na_3-GTP, 10 Na-phosphocreatine, pH 7.3, 290 mOsm for astrocyte

593 recordings. 50 μM AlexaFluor 488 or 594 hydrazide (Thermo Fisher Scientific) was included in

594 the pipette solution to verify cell identity and to position stimulating and puff pipettes. Neurons

595   were voltage clamped at -70 mV and series resistance (R_s) was monitored throughout all

596   recordings and left uncompensated. Experiments were discarded if R_s <30 MΩ and/or changed by

597   >20%. Average R_s was 25.24 ± 0.27 MΩ (n=298 cells).

598

599   *Recordings of synaptic transmission*

600   For all experiments using NMDAR antagonists, 1 mM MK801 was included in the patch pipette

601   solution. Internal solution was allowed to equilibrate into the cell for 10-15 min and inputs were

602   stimulated at a low frequency (0.1Hz) with pairs of pulses at least 45 times before beginning the

603   experiment to pre-block postsynaptic NMDAR receptors. Effective inhibition of NMDAR currents

604   by internal MK801 was confirmed in a separate set of experiments (Figure S1). Pipettes were tip

605   filled with ~0.2 μl of internal solution lacking MK801 to avoid its leakage to the extracellular

606   milieu prior to seal formation. Small bundles of axons in the *stratum radiatum*, *oriens*, or

607   *lacunosum moleulare* were stimulated using AgCl bipolar electrodes in theta-glass pipettes (tip

608   diameter ~2-3 μm) filled with recording aCSF, connected to a stimulus isolation unit (A360, WPI).

609   These bundles are identified throughout as 'input'. Stimulation strengths varied between ~50-

610   500 μA and were adjusted to obtain EPSCs of approximately 50-100 pA. Up to three independent

611   inputs were sampled during a single experiment, though a maximum of two independent inputs

612   were activated per input pathway. When multiple stimulation electrodes were used they were

613   positioned on opposite sides of the neuron and/or in different input pathways (i.e. SR and SLM, or

614   SR and SO). When sampling two inputs in a single pathway, the independence of the two inputs

615   was confirmed by a cross-paired-pulse stimulation paradigm (Letellier et al., 2016); after

616   stimulating one of the two inputs the other input was stimulated in quick succession (50 ms inter-

617   pulse interval). If facilitation or depression was observed in the second pulse, then the position of

618   stimulation electrode was changed and independence of the two inputs was re-assessed. During

619   the experiment, EPSCs from each pathway were sampled with paired pulses every 30 s. Inputs

620   from separate pathways were stimulated at least 5 s apart. EPSCs were sampled over a 10 min

621   baseline period (i.e. 20 sweeps) before the perfusion of drugs and continued for at least an

622   additional 20 min. EPSC amplitudes were averaged over 20 pre-drug baseline sweeps, and 20

623   post-drug sweeps. The change in EPSCs (ΔEPSCs) was calculated as the ratio of the average post-

624   drug amplitude to the average baseline amplitude. PPRs were calculated based on the average

625   EPSCs of 5 sweep bins (i.e. 2.5 min). Baseline and post-drug averages were calculated as the

626   average of four bins (i.e. over 10 min) before and after drug application, respectively. Changes in

627   PPR (ΔPPR) were calculated as the difference between the drug application value and the baseline

628   value. Values for coefficient of variation (CV) were obtained from 20 baseline, and 20 post-drug

629   sweeps. The change in CV^{-2} (ΔCV^{-2}) was calculated as the ratio of post-drug CV^{-2} to pre-drug CV^{-2}.

630   EPSCs and sEPSCs amplitudes in the absence of drug application were stable over the duration of

631 the experiment, and sEPSC amplitudes were stable across all drug conditions tested (Figure S3,
632 S6), suggesting that run-down (i.e. non-stationarities) will not substantially influence the outcome
633 of the CV^{-2} analysis. All EPSC amplitude, rise-time, and decay measurements were performed in
634 Clampfit 10.6 software. sEPSCs were identified as events outside a 50ms window following the
635 second stimulation pulse for each pathway using the template matching algorithm in Clampfit
636 10.6.

637

638 *Astrocyte recordings and NMDA/glycine puff*
639 Astrocytes were identified in acute slices based on mCherry or sulphorhodamine fluorescence, or
640 on their appearance under IR-DIC observation (small, circular cell bodies in the neuropil).
641 Astrocyte identity was always confirmed by their passive electrical properties (linear I-V
642 relationship), low input resistance (<20 MΩ), and low resting membrane potential (< -75 mV), as
643 well as post-hoc labeling by Alexa dyes included in the patch pipette. Recording aCSF contained
644 picrotoxin (100 μM), tetrodotoxin (0.5 μM), and CNQX (10 μM) to reduce network excitability
645 associated with the application of iGluR agonists. Patch pipettes (R_t = 4-6 MΩ) were used to locally
646 deliver recording aCSF solution containing 1 mM NMDA and 1 mM glycine. Puff pipettes were
647 placed approximately 50 μm from the patched cell and puff pressure (3 psi, 100 ms duration) was
648 controlled with a Picospritzer III (Parker Hannifin) connected to N_2 gas.

649

650 *Whole-cell patch RNA extraction from astrocytes and neurons*
651 Whole-cell patch clamp recordings from astrocytes and neurons were performed using pipettes
652 containing (in mM) 130 K gluconate, 10 HEPES, 4 $MgCl_2$, 4 Na_2-ATP, 0.4 Na_3-GTP, 10 Na-
653 phosphocreatine, 1U/μL RNAase inhibitor, 50 μM AlexaFluor488, pH 7.3, 290 mOsm. Pipettes
654 were tip filled (~0.2 μl) with the same internal solution but lacking RNAase inhibitor in order to
655 facilitate obtaining of GΩ seals. After determining the electrical properties of the patched cell to
656 confirm its identity, RNA was extracted using a previously published protocol (Fuzik et al., 2015).
657 The cell was held at -5 mV, and repetitively depolarized to +20 mV for 5 ms at 100 Hz for ~5 min
658 while light negative pressure was applied to the pipette. The AlexaFluor fluorescence signal was
659 visualized to confirm the extraction of cell cytoplasm.

660

661 *Single cell quantitative PCR*
662 Individual patched cells were processed following the provider´s recommendation for the Single
663 Cell-to-CT™ qRT-PCR Kit (ThermoFisher Scientific). cDNAs for GRIN1, GRIN2A, GRIN2B, GRIN2C,
664 GRIN2D and Rn28s1 were quantified by TAQMAN system using the following probes. The
665 provider's recommended pre-amplification step was performed for all the genes except for
666 Rn28s1.

20

667
668 GRIN1 fw 5'GACCGCTTCAGTCCCTTTGG 3', rv 5' CACCTTCCCCAATGCCAGAG 3', probe 5'
669 AGCAGGACGCCCCAGGAAAACCAC 3' (MGBNFQ, 6FAM)
670
671 GRIN2A fw 5' AGACCCCGCTACACACTCTG 3', rv 5'TTGCCCACCTTTTCCCATTCC 3', probe
672 5'AGCACGATCACCACAAGCCTGGGG 3' (MGBNFQ, 6FAM)
673
674 GRIN2B fw 5'GGCATGATTGGTGAGGTGGTC 3', rv 5'GGCTCTAAGAAGGCAGAAGGTG 3', probe
675 5'ATTGCTGCGTGATACCATGACACTGATGCC 3' (MGBNFQ, 6FAM)
676
677 GRIN2C fw 5'GGAGGCTTTCTACAGGCATCTG 3', rv 5'ATACTTCATGTACAGGACCCCATG 3',
678 probe 5'TCCCACCGTCCCACCATCTCCCAG 3' (MGBNFQ, 6FAM)
679
680 GRIN2D fw 5'TCAGCGACCGGAAGTTCCAG 3', rv 5'TCCCTGCCTTGAGCTGAGTG 3', probe
681 5' TCCTCCACTCTTGGCTGGTTGTATCGCA 3'(MGBNFQ, 6FAM)
682
683 Rn28s1 fw 5'CCTACCTACTATCCAGCGAAACC 3', rev 5'AGCTCAACAGGGTCTTCTTTCC 3', probe 5'
684 CTGATTCCGCCAAGCCCGTTCCCT 3' (MGBNFQ, VIC)
685
686 RNA levels were normalized by the quantity of Rn28s1, and standard curves were prepared for

687 estimating the quantity (in femtograms) of the targeted RNAs after pre-amplification. For making

688 the standard curves, total RNA from mouse brain hippocampal tissue was extracted using TRIZOL

689 reagent. Target cDNAs were amplified by regular PCR, and amplicons were purified, quantity of

690 cDNA was measured and submitted to serial dilutions, used for standard curves in TAQMAN

691 system, in parallel to the single cell derived cDNA samples.

692

693 *Intracranial AAV injections*

694 Recombinant AAV vectors were targeted to the dorsal CA1 hippocampus of adult (P60-P90)

695 GRIN1$^{flx/flx}$ mice as previously described (Letellier et al., 2016; Cetin et al., 2007). Bilateral

696 injections (~600 nl/hemisphere at a rate of 200 nl/min) of AAV9.2-GFAP104-nls-mCherry-Cre

697 (6.67×10^{13} genome copies/ml), AAV9.2-GFAP104-nls-mCherry (i.e. ΔCre; 6.86×10^{13} genome

698 copies/ml), AAVDJ8-GFAP104-nls-mCherry-Cre (5.95×10^{13} genome copies/ml), or AAVDJ8-

699 GFAP104-eGFP (also denoted ΔCre for simplicity; 3.98×10^{13} genome copies/ml) were made using

700 the following coordinates; X (posterior from Bregma) – 1.4 mm, Y (lateral from sagittal suture) ±

701 1.4 mm, Z (ventral from pia) – 2.1 mm. Viruses were expressed for at least 21 days (max post-

702 surgical duration of 40 days) before mice were used in physiology or imaging experiments.

703

704 *Immunohistochemistry*

705 Slices prepared from GRIN1$^{flx/flx}$ mice expressing GFAP104-nls-mCherry-Cre were fixed in 4%

706 paraformaldehyde (PFA) in 0.1 M phosphate buffer solution (PB) for 1-2 h, then washed in PB and

707 stored overnight. Alternatively, mice brain tissue was fixed with 4% PFA in PB (pH7.5) by

708 transcardial perfusion, followed by further overnight incubation of the removed brain. Fixed

21

709 brains were cryosectioned to a thickness of 40 μm. Slices were permeabilized with 0.3% Triton X-
710 100 and blocked in 10% goat serum, then incubated in primary antibody overnight at 4°C. Slices
711 were washed and incubated in secondary antibodies for 1-2 h at room temperature. Slices were
712 then washed and mounted in ProLong antifade mounting medium (ThermoFischer Scientific)
713 containing DAPI (1:1000, ThermoFisher Scientific), and visualized on a Zeiss 780, or an Olympus
714 FV1200 or FV3000 confocal microscope. The primary antibodies used were chicken anti-RFP (1:
715 1000, Rockland #600-901-379), mouse anti-GFAP (1:1000, Synaptic Systems #173011), rabbit
716 anti-GFAP (1:500, Abcam ab48050), rabbit anti-NeuN (1:500, Abcam #ab177487), and guinea pig
717 anti-GluN1 (1:100, Alamone Labs AGP-046). The secondary antibodies used were AlexaFluor555
718 goat anti-chicken (1:1000, Invitrogen #A32932), AlexaFluor633 goat anti-mouse (1:1000,
719 Invitrogen #A21052), AlexaFluor 488 goat anti-rabbit (1:1000, Invitrogen #A11034), AlexaFluor
720 488 goat anti-rabbit (1:500, ThermoFischer Scientific), and AlexaFluor 647 goat anti-guinea pig
721 (1:200, Invitrogen A21450).

722

723 *NMDA Receptor immunoprecipitation from mouse brain*
724 Mouse hippocampal tissues were dissociated using a glass dounce homogenizer in a 50 mM Tris-
725 HCl, pH 9.0 buffer containing protease inhibitors (10% w/v, cOmplete™, Merck). Subsequently,
726 1% (w/v) sodium deoxycholate was added and incubated for 30 min at 37°C with mild shaking to
727 solubilize the tissue. Samples were centrifuged at 100,000 rpm at 4°C for 1h. Supernatant was
728 collected, protein concentration was measured by the BCA assay, and stored at -80°C for later
729 analysis or diluted 5-fold in a 50 mM Tris-HCl pH 7.5 buffer containing 0.1% of Triton X-100 for
730 co-immunoprecipitation experiments.

731 To test for co-immunoprecipitation, a mix of Sepharose Fast-Flow protein A and protein G
732 beads was prepared. For each antibody reaction, 40 μl of the mixed resin was incubated with 5 μg
733 of antibody. After at least 2 h of incubation at 4°C excess antibody was removed by washing, and
734 2 mg of protein extract was added to each sample containing the resin beads bound by the
735 antibody and incubated overnight at 4°C. Resins were washed 3 times with 10 volumes of 50 mM
736 Tris-HCl pH 7.5 with 0.1% Triton X-100. Supernatant was carefully removed, and resins were
737 suspended in 2x SDS-PAGE protein loading buffer containing DTT. The unbound protein extract
738 was treated for a second overnight incubation at 4°C with a freshly prepared antibody-bound
739 resin under identical conditions as the first overnight incubation, to ensure effective pull-down of
740 soluble NMDA receptor content from the extract. Co-immunoprecipitated proteins from the two
741 rounds of incubation were pooled together.

742 Protein samples (inputs and co-immunoprecipitated proteins) were heat denatured for 2
743 min at 95°C, and subjected to 6% SDS-PAGE separation followed by western blot. Antibodies used
744 were: mouse anti-NR1 (Synaptic Systems #114011), rabbit anti-GluN2A/2B (Synaptic Systems

22

745 #244003), rabbit anti-GluN2C (generously provided by Dr. Masahiko Watanabe or purchased

746 from Frontier Institute #GLURE3C-RB-AF270), mouse anti-Cre (Merck Millipore clone 2D8) and

747 mouse anti-BirA (Novus biologicals #NBP2-59939).

748

749 *Mathematical Model for the Numerical Investigation*

750 We used the facilitation model based on the Tsodyks-Pawelzik-Markram model (Tsodyks

751 et al., 1998) to reproduce ratios of peaks of excitatory postsynaptic current (EPSC) with a 20-Hz

752 spike input. The synaptic dynamics is modeled by [1]:

$$\frac{dx_0(t)}{dt} = \frac{x_2(t)}{\tau_{rec}} - u_0(t_{sp}^+)x_0(t_{sp}^-)\delta(t - t_{sp}) \tag{1}$$

$$\frac{dx_1(t)}{dt} = -\frac{x_1(t)}{\tau_{in}} + u_0(t_{sp}^+)x_0(t_{sp}^-)\delta(t - t_{sp}) \tag{2}$$

759

$$\frac{dx_2(t)}{dt} = \frac{x_1(t)}{\tau_{in}} - \frac{x_2(t)}{\tau_{rec}} \tag{3}$$

$$\frac{du_0(t)}{dt} = -\frac{u_0(t)}{\tau_f} + U_{SE}\left(1 - u_0(t_{sp}^-)\right)\delta(t - t_{sp}). \tag{4}$$

753 Here x_0 is the portion of available neurotransmitters, $x_1(t)$ is the portion of neurotransmitters

754 released by pre-synaptic spikes, $x_2(t)$ is the portion of neurotransmitters being recovered, $u_0(t)$

755 is the utilization of available neurotransmitters after each spike. τ_{in} is the timescale of

756 neurotransmitters release. τ_{rec} is the recovery timescale. τ_f is the timescale of synaptic

757 facilitation. U_{SE} is the initial release probability without the influence of synaptic facilitation. In

758 this model, the dynamical variables are x_i with $x_0 + x_1 + x_2 = 1$.

760 There are four parameters to be determined: τ_f, τ_{rec}, U_{SE} and $w(0)$, where $w(0)$ is the

761 initial connection weight between neurons. For simplicity, $w(0)$ is evenly distributed among 10

762 synapses (Gal et al., 2017). U_{SE} is a random number drawn from a log-normal distribution, in

763 which the distribution is given by

$$P(U_{SE}) = \frac{1}{U_{SE}\sigma\sqrt{2\pi}} \exp\left[-\frac{(\ln|U_{SE}| - \mu)^2}{2\sigma_{max}^2}\right] \tag{5}$$

764

$$\sigma_{max} = \frac{-2 + \sqrt{4 - 4\ln|U_{max}|}}{2a} \tag{6}$$

$$\mu = \ln|U_{max}| + \sigma_{max}^2. \tag{7}$$

765

766 The distribution of release probability in current work was taken from Murthy et al. (1997), which

767 was denoted by U_{SE}. In simulations we use a long-normal function to model the distribution (cf.

768 Figure 3A).

769 To compare with experimental result, the excitatory postsynaptic current (EPSC) was

770 defined as $I(t) = w(0)x_1(t)$. The best fit to the experimental data is shown in Figure S8A where

771 the best-fit parameters are τ_f = 540 ms, τ_{rec} = 20 ms, U_{max} = 0.1 and $w(0)$ = 332.

23

772   The BCM-like learning rule for investigation is given by

$$I(t) = w(t)x_1(t) \tag{8}$$

773

$$\tau_w \frac{dw(t)}{dt} = I(t)[I(t) - \theta(t)^2]x_1(t) \tag{9}$$

$$\tau_\theta \frac{d\theta(t)}{dt} = \alpha I(t) - \theta(t). \tag{10}$$

774 Here θ is the threshold to stop the change of w, while τ_θ is the timescale to integrate the
775 postsynaptic current $I(t)$. τ_w is the timescale of $w(t)$. α is a parameter to be chosen for different
776 scenarios: LTP or LTD. In this study, the following values were used: τ_w = 100 ms and τ_θ = 10 ms.
777 The equations (8) to (10) constitute the BCM learning rule (Bienenstock et al., 1982).
778   In the series of comparisons shown in Figure 3C, the changes in synaptic plasticity as
779 defined   by

780

$$w\left(t = 2\min, \sigma = \frac{\sigma_{max}}{2}\right) - w(t = 2\min, \sigma = \sigma_{max}) \quad \text{for LTP} \tag{11}$$

$$w(t = 2\min, \sigma = \sigma_{max}) - w\left(t = 2\min, \sigma = \frac{\sigma_{max}}{2}\right) \quad \text{for LTD} \tag{12}$$

781 are represented as a function of the absolute change in the connection weight in the control
782 release probability distribution condition as defined by $(w(t = 2\min, \sigma = \sigma_{max}) - w(t = 0))$.
783 Note that the comparison at $t = 2$ min was to compare $w(t)$ after the epoch of paired stimulations.
784 Note also that $\sigma = \frac{\sigma_{max}}{2}$ represents the cases of NMDARs blocked, while $\sigma = \sigma_{max}$ represents the
785 control cases. In Figure 3C, the reduction in σ always degrades the efficacy of LTD; however, the
786 efficacy of LTP may vary for different level of LTP. For the relative change in $w(t) \lesssim 0.06$, the
787 reduction of σ does not degrade the LTP efficacy whereas for the relative change in $w(t) \gtrsim 0.06$,
788 the reduction in σ degrades the LTP efficacy.
789   In the model and simulation based on leaky integrate-and-fire (LIF) neurons, two neurons
790 are connected by 10 synapses. The neurons have time constant $\tau = 15$ ms, threshold potential
791 $V_{thre} = -50.0$ mV, reversal potential $E_L = -65.0$ mV and refractory time $\tau_{ref} = 2$ ms. The rising
792 synaptic time constant is 2 ms and decay time constant is ~5 ms. The synaptic model is the same
793 as equations (1) – (4), and the probability distribution was the same as equations (5) – (7). The
794 best-fit of the model to the data is shown in Figure S8B, where the parameters are τ_f = 980 ms,
795 τ_{rec} = 25 ms, U_{max} = 0.1 and $w(0)$ = 6.7.
796
797 *Statistics*
798 All statistical analyses were performed using OriginPro software (OriginLab Corp.). Datasets were
799 tested for normality using the Shapiro Wilk test. When the criteria for normality was achieved,
800 differences of mean values were examined using paired or unpaired Student's two-tailed t-tests
801 or one-way ANOVAs. When the criteria for normality was not achieved, differences in mean values
802 were examined using Mann-Whitney or Kruskal Wallis tests. Normalized mean values obtained

24

803   from recordings (i.e. normalized EPSCs) were compared to values obtained at the same timepoint

804   in control experiments using Mann-Whitney tests. Variance of PPR distributions were examined

805   using one-tailed f-tests for equal variances or Levene's test. Box plots represent median and

806   quartile values, whiskers represent maximum and minimum values that are not outliers. P values

807   are indicated throughout or indicated by * if $p < 0.05$.

Acknowledgements

Author Contributions

PHC and YG designed the project and wrote the manuscript. PHC performed electrophysiology experiments and analyzed data. CCAF and TF contributed mathematical modeling and simulation and wrote the manuscript. PHC and AK isolated astrocyte and neuronal RNA for RT-PCR experiments. APF performed biochemistry and RT-PCR experiments. MA and KS made the GluN2C-Cre mice. APF, and AT and MK performed immunohistochemistry experiments. SGG constructed and MK prepared viral reagents.

Competing interests

The authors declare no competing interests.

References

Abbott, L.F., and Regehr, W.G. (2004). Synaptic computation. Nature *431*, 796–803.

Abe, M., Fukaya, M., Yagi, T., Mishina, M., Watanabe, M., and Sakimura, K. (2004). NMDA receptor GluRepsilon/NR2 subunits are essential for postsynaptic localization and protein stability of GluRzeta1/NR1 subunit. J. Neurosci. *24*, 7292-7304.

Alsaad, H.A., DeKorver, N.W., Mao, Z., Dravid, S.M., Arikkath, J., and Monaghan, D.T. (2019). In the Telencephalon, GluN2C NMDA Receptor Subunit mRNA is Predominately Expressed in Glial Cells and GluN2D mRNA in Interneurons. Neurochem Res. *44*, 61-77.

Amaral, D.G., and Lavenex, P. (2006). Hippocampal neuroanatomy. In The Hippocampus Book, P. Andersen, R. Morris, D. Amaral, T. Bliss, J. O'Keefe, eds. (Oxford, UK: Oxford University Press, Oxford), pp. 37-114.

Andrade-Talavera, Y., Duque-Feria, P., Paulsen, O., and Rodríguez-Moreno, A. (2016). Presynaptic Spike Timing-Dependent Long-Term Depression in the Mouse Hippocampus. Cereb

26

Cortex *26*, 3637-3654.

Araque, A., Carmignoto, G., Haydon, P.G., Oliet, S.H., Robitaille, R., and Volterra, A. (2014). Gliotransmitters travel in time and space. Neuron *81*, 728-739.

Attwell, D., Buchan, A.M., Charpak, S., Lauritzen, M., Macvicar, B.A., and Newman, E.A. (2010). Glial and neuronal control of brain blood flow. Nature *468*, 232–243.

Atwood, H.L., and Karunanithi, S. (2002). Diversification of synaptic strength: presynaptic elements. Nat. Rev. Neurosci. *3***,** 497–516.

Barbour, B., Brunel, N., Hakim, V., and Nadal, J.P. (2007). What can we learn from synaptic weight distributions? Trends Neurosci. *30*, 622-629.

Bazargani, N., and Attwell, D. (2016). Astrocyte calcium signaling: the third wave. Nature *19***,** 182–189.

Bender, K.J,, Allen, C.B., Bender, V.A., and Feldman, D.E. (2006). Synaptic basis for whisker deprivation-induced synaptic depression in rat somatosensory cortex. J. Neurosci. *26*, 4155-4165.

Bezaire, M.J., and Soltesz I. (2013). Quantitative assessment of CA1 local circuits: knowledge base for interneuron-pyramidal cell connectivity. Hippocampus *23*, 751-785.

Bienenstock, E.L., Cooper, L.N., and Munro, P.W. (1982). Theory for the development of neuron selectivity: orientation specificity and binocular interaction in visual cortex. J. Neurosci. *2*, 32-48.

Bindocci, E., Savtchouk, I., Liaudet, N., Becker, D., Carriero, G., and Volterra, A. (2017). Three-dimensional Ca^{2+} imaging advances understanding of astrocyte biology. Science *356*, eaai8185.

Bliss, T.V., and Collingridge, G.L. (1993). A synaptic model of memory: Long-term potentiation in the hippocampus. Nature *361*, 31–39.

Boisvert, M.M., Erikson, G.A., Shokhirev, M.N., and Allen, N.J. (2018). The Aging Astrocyte Transcriptome from Multiple Regions of the Mouse Brain. Cell Rep. *22*, 269-285.

Branco, T., Staras, K., Darcy, K.J., and Goda, Y. (2008). Local Dendritic Activity Sets Release Probability at Hippocampal Synapses. Neuron *59*, 475–485.

Branco, T., and Staras, K. (2009). The probability of neurotransmitter release: variability and feedback control at single synapses. Nat. Rev. Neurosci. *10*, 373-383.

Brenowitz, S.D., and Regehr, W.G. (2007). Reliability and Heterogeneity of Calcium Signaling at Single Presynaptic Boutons of Cerebellar Granule Cells. J. Neurosci. *27*, 7888–7898.

Bromer, C., Bartol, T.M., Bowden, J.B., Hubbard, D.D., Hanka, D.C., Gonzalez, P.V., Kuwajima, M., Mendenhall, J.M., Parker, P.H., Abraham, W.C., Sejnowski, T.J., and Harris, K.M. (2018). Long-term potentiation expands information content of hippocampal dentate gyrus synapses. Proc Natl Acad Sci. USA 115, E2410–E2418.

Brunel, N. (2016). Is cortical connectivity optimized for storing information? Nat. Neurosci. *19*, 749-755.

Burke, K.J. Jr., Keeshen, C.M., and Bender, K.J. (2018). Two Forms of Synaptic Depression Produced by Differential Neuromodulation of Presynaptic Calcium Channels. Neuron *99*, 969-984.

Buzsáki, G., and Mizuseki, K. (2014). The log-dynamic brain: how skewed distributions affect network operations. Nat. Rev. Neurosci. *15*, 264–278.

Cetin, A., Komai, S., Eliava, M., Seeburg, P.H., and Osten, P. (2007). Stereotaxic gene delivery in the rodent brain. Nat Protoc *1*, 3166–3173.

Chai, H., Diaz-Castro, B., Shigetomi, E., Monte, E., Octeau, J.C., Yu, X., Cohn, W., Rajendran, P.S., Vondriska, T.M., Whitelegge, J.P., Coppola, G., and Khakh, B.S. (2017). Neural Circuit-Specialized Astrocytes: Transcriptomic, Proteomic, Morphological, and Functional Evidence. Neuron *95*, 531–549.

Chen, J., Tan, Z., Zeng, L., Zhang, X., He, Y., Gao, W., Wu, X., Li, Y., Bu, B., Wang, W., and Duan, S. (2013). Heterosynaptic long-term depression mediated by ATP released from astrocytes. Glia *61*, 178-191.

Chung, W.S., Welsh, C.A., Barres, B.A., and Stevens, B. (2015). Do glia drive synaptic and cognitive impairment in disease? Nat Neurosci *18*, 1539-1545.

Clarke, L.E., and Barres, B.A. (2013). Emerging roles of astrocytes in neural circuit development. Nat. Rev. Neurosci. *14*, 311-321.

Collingridge, G.L., Peineau, S., Howland, J.G., and Wang, Y.T. (2010). Long-term depression in the CNS. Nat. Rev. Neurosci. 11, 459-473.

Covelo, A., and Araque, A. (2018). Neuronal activity determines distinct gliotransmitter release from a single astrocyte. Elife *7*, e32237.

Cui, Y., Yang, Y., Ni, Z., Dong, Y., Cai, G., Foncelle, A., Ma, S., Sang, K., Tang, S., Li, Y., Shen, Y., Berry, H., Wu, S., and Hu, H. (2018). Astroglial Kir4.1 in the lateral habenula drives neuronal bursts in depression. Nature *554*, 323-327.

Dallérac, G., Zapata, J., and Rouach, N. (2018). Versatile control of synaptic circuits by astrocytes: where, when and how? Nat. Rev. Neurosci. *19*, 729-743.

Deemyad, T., Lüthi, J., and Spruston, N. (2018). Astrocytes integrate and drive action potential firing in inhibitory subnetworks. Nat. Commun. *9*, 4336.

Di Castro, M.A., Chuquet, J., Liaudet, N., Bhaukaurally, K., Santello, M., Bouvier, D., Tiret, P., and Volterra, A. (2011) Local Ca^{2+} detection and modulation of synaptic release by astrocytes. Nat. Neurosci. *14*, 1276–1284.

Dobrunz, L.E., and Stevens, C.F. (1997). Heterogeneity of release probability, facilitation, and depletion at central synapses. Neuron *18*, 995–1008.

Dore, K., Stein, I.S., Brock, J.A., Castillo, P.E., Zito, K., and Sjöström, P.J. (2017). Unconventional NMDA Receptor Signaling. J. Neurosci. *37*, 10800–10807.

Éltes, T., Kirizs, T., Nusser, Z., and Holderith, N. (2017). Target cell type-dependent differences in Ca2+ channel function underlie distinct release probabilities at hippocampal glutamatergic terminals. J. Neurosci. *37*, 1910–1924.

Feldman, D.E., and Brecht, M. (2005). Map plasticity in somatosensory cortex. Science *310*, 810-815.

Fischer, G., Mutel, V., Trube, G., Malherbe, P., Kew, J.N., Mohacsi, E., Heitz, M.P., and Kemp, J.A . (1997). Ro 25-6981, a highly potent and selective blocker of N-methyl-D-aspartate receptors containing the NR2B subunit. Characterization in vitro. J. Pharmacol. Exp. Ther. *283*, 1285–1292.

Fukaya, M., Kato, A., Lovett, C., Tonegawa, S., and Watanabe, M. (2003). Retention of NMDA receptor NR2 subunits in the lumen of endoplasmic reticulum in targeted NR1 knockout mice. Proc. Natl. Acad. Sci. USA *100*, 4855–4860.

Fulterer, A., Andlauer, T.F.M., Ender, A., Maglione, M., Eyring, K., Woitkuhn, J., Lehmann, M., Matkovic-Rachid, T., Geiger, J.R.P., Walter, A.M., Nagel, K.I., and Sigrist, S.J. (2018). Active Zone Scaffold Protein Ratios Tune Functional Diversity across Brain Synapses. Cell Reports *23*, 1259–1274.

Fuzik, J., Zeisel, A., Máté, Z., Calvigioni, D., Yanagawa, Y., Szabó, G., Linnarsson, S., and Harkany, T. (2015). Integration of electrophysiological recordings with single-cell RNA-seq data identifies neuronal subtypes. Nat. Biotechnol. *34*, 175–183.

Gal, E., London, M., Globerson, A., Ramaswamy, S., Reimann, M.W., Muller, E., Markram, H., and Segev, I. (2017). Rich cell-type-specific network topology in neo-cortical microcircuitry. Nat. Neurosci. *20*, 1004-1013.

Gasparini, F., Lingenhöhl, K., Stoehr, N., Flor, P.J., Heinrich, M., Vranesic, I., Biollaz, M., Allgeier, H., Heckendorn, R., Urwyler, S., Varney, M.A., Johnson, E.C., Hess, S.D., Rao, S.P., Sacaan, A.I., Santori, E.M., Veliçelebi, G., and Kuhn, R. (1999). 2-Methyl-6-(phenylethynyl)-pyridine (MPEP), a potent, selective and systemically active mGlu5 receptor antagonist. Neuropharmacology *38*, 1493-1503.

Giaume, C., Koulakoff, A., Roux, L., Holcman, D., and Rouach, N. (2010). Astroglial networks: a step further in neuroglial and gliovascularinteractions. Nat. Rev. Neurosci. *11*, 87-99.

Glebov, O.O., Jackson, R.E., Winterflood, C.M., Owen, D.M., Barker, E.A., Doherty, P., Ewers, H., and Burrone, J . (2017). Nanoscale Structural Plasticity of the Active Zone Matrix Modulates Presynaptic Function. Cell Reports *18*, 2715–2728.

Goda, Y., and Stevens, C.F. (1998). Readily releasable pool size changes associated with long term

depression. Proc. Natl. Acad. Sci. USA *95*, 1283–1288.

Gottlieb, M., and Matute, C. (1997). Expression of ionotropic glutamate receptor subunits in glial cells of the hippocampal CA1 area following transient forebrain ischemia. J Cereb Blood Flow Metab. *17*, 290-300.

Graham, W.V., Bonito-Oliva, A., and Sakmar, T.P. (2017). Update on Alzheimer's Disease Therapy and Prevention Strategies. Annu. Rev. Med. *68*, 413-430.

Gupta, S.C., Ravikrishnan, A., Liu, J., Mao, Z., Pavuluri, R., Hillman, B.G., Gandhi, P.J., Stairs, D.J., Li, M., Ugale, R.R., Monaghan, D.T., and Dravid, S.M. (2016). The NMDA receptor GluN2C subunit controls cortical excitatory-inhibitory balance, neuronal oscillations and cognitive function. Sci Rep. *6*, 38321.

Hansen, K. B., and Traynelis, S.F. (2011). Structural and mechanistic determinants of a novel site for noncompetitive inhibition of GluN2D-containing NMDA receptors. J. Neurosci. *31*, 3650–3661.

Hansen, K.B., Yi, F., Perszyk, R.E., Furukawa, H., Wollmuth, L.P., Gibb, A.J., and Traynelis, S.F. (2018). Structure, function, and allosteric modulation of NMDA receptors. J. Gen. Physiol. *150*, 1081-1105.

Hansen, K.B., Yi, F., Perszyk, R.E., Menniti, F.S., and Traynelis, S.F. (2017). NMDA Receptors in the Central Nervous System. Methods Mol. Biol. *1677*, 1-80.

Hillman, B.G., Gupta, S.C., Stairs, D.J., Buonanno, A., Dravid, S.M. (2011). Behavioral analysis of NR2C knockout mouse reveals deficit in acquisition of conditioned fear and working memory. Neurobiol Learn Mem. *95*, 404-414.

Holderith, N., Lorincz, A., Katona, G., Rózsa, B., Kulik, A., Watanabe, M., and Nusser, Z. (2012). Release probability of hippocampal glutamatergic terminals scales with the size of the active zone. Nat. Neurosci. *15*, 988–997.

Jourdain, P., Bergersen, L.H., Bhaukaurally, K., Bezzi, P., Santello, M., Domercq, M., Matute, C., Tonello, F., Gundersen, V., and Volterra, A. (2007). Glutamate exocytosis from astrocytes controls synaptic strength. Nat. Neurosci. *10*, 331–339.

Káradóttir, R., Cavelier, P., Bergersen, L.H., and Attwell, D. (2005). NMDA receptors are expressed in oligodendrocytes and activated in ischaemia. Nature *438*, 1162-1166.

Karavanova, I., Vasudevan, K., Cheng, J., and Buonanno, A. (2007). Novel regional and developmental NMDA receptor expression patterns uncovered in NR2C subunit-β-galactosidase knock-in mice. Molecular and Cellular Neuroscience *34*, 468–480.

Khakh, B.S., and Sofroniew, M.V. (2015). Diversity of astrocyte functions and phenotypes in neural circuits. Nat. Neurosci. *18*, 942–952.

Kirchhoff, F. (2017) Analysis of Functional NMDA Receptors in Astrocytes. Methods Mol Biol *1677*, 241-251.

Kotermanski, S.E., and Johnson, J.W. (2009). Mg^{2+} imparts NMDA receptor subtype selectivity to the Alzheimer's drug memantine. J. Neurosci. *29*, 2774-2779.

Krebs, C., Fernandes, H.B., Sheldon, C., Raymond, L.A., and Baimbridge, K.G. (2003) Functional NMDA receptor subtype 2B is expressed in astrocytes after ischemia in vivo and anoxia in vitro. J. Neurosci. *23*, 3364–3372.

Krystal, J.H., Abdallah, C.G., Sanacora, G., Charney, D.S., and Duman, R.S. (2019). Ketamine: A Paradigm Shift for Depression Research and Treatment. Neuron *101*, 774-778.

Lalo, U., Pankratov, Y., Kirchhoff, F., North, R.A., and Verkhratsky, A. (2006). NMDA receptors mediate neuron-to-glia signaling in mouse cortical astrocytes. Journal of Neuroscience *26*, 2673–2683.

Lanjakornsiripan, D., Pior, B.J., Kawaguchi, D., Furutachi, S., Tahara, T., Katsuyama, Y., Suzuki, Y., Fukazawa, Y., and Gotoh, Y. (2018). Layer-specific morphological and molecular differences in neocortical astrocytes and their dependence on neuronal layers. Nat. Commun. *9*, 1623.

Larkman, A., Hannay, T., Stratford, K., and Jack, J. (1992). Presynaptic release probability influences the locus of long-term potentiation. Nature *360*, 70–73.

Letellier, M. Park, Y.K., Chater, T.E., Chipman, P.H., Gautam, S.G., Oshima-Takago, T., and Goda, Y. (2016). Astrocytes regulate heterogeneity of presynaptic strengths in hippocampal networks. Proc. Natl. Acad. Sci. USA *113*, E2685-94.

Lines, J., Covelo, A., Gómez, R., Liu, L., and Araque, A. (2017). Synapse-specific regulation revealed at single synapses is concealed when recording multiple synapses. Front. Cell. Neurosci. *11*:367.

Madisen, L., Zwingman, T.A., Sunkin, S.M., Oh, S.W., Zariwala, H.A., Gu, H., Ng, L.L., Palmiter, R.D., Hawrylycz, M.J., Jones, A.R., Lein, E.S., and Zeng, H. (2010). A robust and high-throughput Cre reporting and characterization system for the whole mouse brain. Nat Neurosci. *13*, 133-140.

Malenka RC, Bear MF. (2004). LTP and LTD: an embarrassment of riches. Neuron *44*, 5-21.

Malinow, R., and Tsien, R.W. (1990). Presynaptic enhancement shown by whole-cell recordings of long-term potentiation in hippocampal slices. Nature *346*, 177–180.

Mao, Z., Mao, Z., He, S., Mesnard, C., Synowicki, P., Zhang, Y., Chung, L., Wiesman, A.I., Wilson, T.W., and Monaghan, D.T. (2020). NMDA receptors containing GluN2C and GluN2D subunits have opposing roles in modulating neuronal oscillations; potential mechanism for bidirectional feedback. Brain Res. *1727*, 146571.

Markram, H., and Sakmann, B. (1995). Action potentials propagating back into dendrites triggers changes in efficacy. Society of Neuroscience Abstract. 21.

Markram, H., Wang, Y., and Tsodyks, M. (1998). Differential signaling via the same axon of

neocortical pyramidal neurons. Proc. Natl. Acad. Sci. USA *95*, 5323–5328.

Marra, V., Burden, J.J., Thorpe, J.R., Smith, I.T., Smith, S.L., Häusser, M., Branco, T., and Staras, K. (2012). A Preferentially Segregated Recycling Vesicle Pool of Limited Size Supports Neurotransmission in Native Central Synapses. Neuron *76*, 579-589.

Martín, R., Bajo-Grañeras, R., Moratalla, R., Perea, G., and Araque, A. (2015). Circuit-specific signaling in astrocyte-neuron networks in basal ganglia pathways. Science *349*, 730–734.

Martin-Fernandez, M., Jamison, S., Robin, L.M., Zhao, Z., Martin, E.D., Aguilar, J., Benneyworth, M.A., Marsicano, G., and Araque, A. (2017). Synapse-specific astrocyte gating of amygdala-related behavior. Nat. Neurosci. *20*, 1540–1548.

Matz, J., Gilyan, A., Kolar, A., McCarvill, T, and Krueger, S.R. (2010). Rapid structural alterations of the active zone lead to sustained changes in neurotransmitter release. Proc. Natl. Acad. Sci. USA. *107*, 8836-8841.

Miyazaki, T., Yamasaki, M., Hashimoto, K., Yamazaki, M., Abe, M., Usui, H., Kano, M., Sakimura, K., and Watanabe, M. (2012). Cav2.1 in cerebellar Purkinje cells regulates competitive excitatory synaptic wiring, cell survival, and cerebellar biochemical compartmentalization. J Neurosci. *32*, 1311-1328.

Murthy, V.N., Sejnowski, T.J., and Stevens, C.F. (1997). Heterogeneous release properties of visualized individual hippocampal synapses. Neuron *18*, 599-612.

Murphy-Royal, C., Dupuis, J.P., Varela, J.A., Panatier, A., Pinson, B., Baufreton, J., Groc, L., and Oliet, S.H. (2015). Surface diffusion of astrocytic glutamate transporters shapes synaptic transmission. Nat. Neurosci. *18*, 219–226.

Navarrete, M., Cuartero, M.I., Palenzuela, R., Draffin, J.E., Konomi, A., Serra, I., Colié, S., Castaño-Castaño, S., Hasan, M.T., Nebreda, Á.R., and Esteban, J.A. (2019). Astrocytic p38α MAPK drives NMDA receptor-dependent long-term depression and modulates long-term memory. Nat. Commun. *10*, 2968.

Nicoll, R.A. (2017). A brief history of long-term potentiation. Neuron *93*, 281-290.

Nimmerjahn, A., Kirchhoff, F., Kerr, J.N., and Helmchen, F. (2004). Sulforhodamine 101 as a specific marker of astroglia in the neocortex in vivo. Nat. Methods *1*, 31-37.

Paoletti, P., Bellone, C., and Zhou, Q. (2013). NMDA receptor subunit diversity: impact on receptor properties, synaptic plasticity and disease. Nat. Rev. Neurosci. *14*, 383-400.

Panatier, A., Vallée, J., Haber, M., Murai, K.K., Lacaille, J.C., and Robitaille, R. (2011). Astrocytes Are Endogenous Regulators of Basal Transmission at Central Synapses. Cell *146*, 785–798.

Pannasch, U., Freche, D., Dallérac, G., Ghézali, G., Escartin, C., Ezan, P., Cohen-Salmon, M., Benchenane, K., Abudara, V., Dufour, A., Lübke, J.H., Déglon, N., Knott, G., Holcman,

32

D., and Rouach, N. (2014). Connexin 30 sets synaptic strength by controlling astroglial synapse invasion. Nat. Neurosci. *17*, 549–558.

Park, H., Li, Y., and Tsien, R.W. (2012). Influence of Synaptic Vesicle Position on Release Probability and Exocytotic Fusion Mode. Science *335*, 1362–1366.

Pascual, O., Casper, K.B., Kubera, C., Zhang, J., Revilla-Sanchez, R., Sul, J.Y., Takano, H., Moss, S.J., McCarthy, K., and Haydon, P.G. (2005). Astrocytic Purinergic Signaling Coordinates Synaptic Networks. Science *310*, 113–116.

Perea, G., and Araque, A. (2007). Astrocytes Potentiate Transmitter Release at Single Hippocampal Synapses. Science *317*, 1083–1086.

Pinto-Duarte, A., Roberts, A.J., Ouyang, K., and Sejnowski, T.J. (2019). Impairments in remote memory caused by the lack of Type 2 IP$_3$ receptors. Glia *67*, 1976-1989.

Ravikrishnan, A., Gandhi, P.J., Shelkar, G.P., Liu, J., Pavuluri, R., and Dravid, S.M. (2018). Region-specific Expression of NMDA Receptor GluN2C Subunit in Parvalbumin-Positive Neurons and Astrocytes: Analysis of GluN2C Expression using a Novel Reporter Model. Neurosci. *380*, 49–62.

Reyes, A., Lujan, R., Rozov, A., Burnashev, N., Somogyi, P., and Sakmann, B. (1998). Target-cell-specific facilitation and depression in neocortical circuits. Nat. Neurosci. *1*, 279–285.

Rotman, Z., and Klyachko, V.A. (2013). Role of synaptic dynamics and heterogeneity in neuronal learning of temporal code. J. Neurophysiol. *110*, 2275–2286.

Royer, S., and Paré, D. (2003). Conservation of total synaptic weight through balanced synaptic depression and potentiation. Nature *422*, 518-522.

Saab, A.S., Tzvetavona, I.D., Trevisiol, A., Baltan, S., Dibaj, P., Kusch, K., Möbius, W., Goetze, B., Jahn, H.M., Huang, W., Steffens, H., Schomburg, E.D., Pérez-Samartín, A., Pérez-Cerdá, F., Bakhtiari, D., Matute, C., Löwel, S., Griesinger, C., Hirrlinger, J., Kirchhoff, F., and Nave, K.A. (2016). Oligodendroglial NMDA Receptors Regulate Glucose Import and Axonal Energy Metabolism. Neuron *91*, 119-132.

Sakers, K., Lake, A.M., Khazanchi, R., Ouwenga, R., Vasek, M.J., Dani, A., and Dougherty, J.D. (2017). Astrocytes locally translate transcripts in their peripheral processes. Proc. Natl. Acad. Sci. USA *114*, E3830-E3838.

Santello, M., Toni, N., and Volterra, A. (2019). Astrocyte function from information processing to cognition and cognitive impairment. Nat Neurosci. *22*, 154-166.

Sanz-Clemente, A., Nicoll, R.A., and Roche, K.W. (2013). Diversity in NMDA receptor composition: many regulators, many consequences. Neuroscientist *19*, 62-75.

Schipke, C.G., Ohlemeyer, C., Matyash, M., Nolte, C., Kettenmann, H., and Kirchhoff, F. (2001). Astrocytes of the mouse neocortex express functional N-methyl-D-aspartate

33

receptors. FASEB J *15*, 1270-1272.

Schroeder, A., Vanderlinden, J., Vints, K., Ribeiro, L.F., Vennekens, K.M., Gounko, N.V., Wierda, K.D., and de Wit, J. (2018). A Modular Organization of LRR Protein-Mediated Synaptic Adhesion Defines Synapse Identity. Neuron *99*, 329-344.

Schwarz, Y., Zhao, N., Kirchhoff, F., and Bruns, D. (2017). Astrocytes control synaptic strength by two distinct v-SNARE-dependent release pathways. Nat. Neurosci. *20*, 1529-1539.

Serrano, A., Robitaille, R., and Lacaille, J.-C. (2008). Differential NMDA-dependent activation of glial cells in mouse hippocampus. Glia *56*, 1648–1663.

Shih, P.-Y., Savtchenko, L.P., Kamasawa, N., Dembitskaya, Y., McHugh, T.J., Rusakov, D.A., Shigemoto, R., and Semyanov, A. (2013). Retrograde Synaptic Signaling Mediated by K+ Efflux through Postsynaptic NMDA Receptors. Cell Rep. *5*, 941–951.

Simard, M., and Nedergaard, M. (2004). The neurobiology of glia in the context of water and ion homeostasis. Neuroscience *129*, 877–896.

Sun, W., McConnell, E., Pare, J.F., Xu, Q., Chen, M., Peng, W., Lovatt, D., Han, X., Smith, Y., and Nedergaard, M. (2013). Glutamate-dependent neuroglial calcium signaling differs between young and adult brain. Science *339*, 197–200.

Tan, Z., Liu, Y., Xi, W., Lou, H.F., Zhu, L., Guo, Z., Mei, L., and Duan, S. (2017). Glia-derived ATP inversely regulates excitability of pyramidal and CCK-positive neurons. Nat. Commun. *8*, 13772.

Thalhammer, A., Contestabile, A., Ermolyuk, Y.S., Ng, T., Volynski, K.E., Soong, T.W., Goda, Y., and Cingolani, L.A. (2017). Alternative Splicing of P/Q-Type Ca^{2+} Channels Shapes Presynaptic Plasticity. Cell Rep. *20*, 333–343.

Tsodyks, M., Pawelzik, K., and Markram, H. (1998). Neural networks with dynamic synapses. Neural Comput. *10*, 821-835.

Turrigiano, G.G. (2017). The dialectic of Hebb and homeostasis. Philos. Trans. R. Soc. Lond. B Biol. Sci. *372*, pii: 20160258.

Vitureira, N., and Goda, Y. (2013). Cell biology in neuroscience: the interplay between Hebbian and homeostatic synaptic plasticity. J. Cell Biol. *203*, 175-186.

Watanabe, M., Inoue, Y., Sakimura, K., Mishina, M. (1993). Distinct distributions of five N-methyl-D-aspartate receptor channel subunit mRNAs in the forebrain. J. Comp. Neurol. *338*, 377-390.

Williams, N.R., and Schatzberg, A.F. (2016). NMDA antagonist treatment of depression. Curr. Opin. Neurobiol. *36*, 112-117.

Zenke, F., and Gerstner, W. (2017). Hebbian plasticity requires compensatory processes on multiple timescales. Philos. Trans. R. Soc. Lond. B Biol. Sci. *372*, pii: 20160259.

Zhang, J.-M., Wang, H.K., Ye, C.Q., Ge, W., Chen, Y., Jiang, Z.L., Wu, C.P., Poo, M.M., and Duan, S.

(2003). ATP released by astrocytes mediates glutamatergic activity-dependent heterosynaptic suppression. Neuron *40*, 971–982.

Zhang, Y., Chen, K., Sloan, S.A., Bennett, M.L., Scholze, A.R., O'Keeffe, S., Phatnani, H.P., Guarnieri, P., Caneda, C., Ruderisch, N., Deng, S., Liddelow, S.A., Zhang, C., Daneman, R., Maniatis, T., Barres, B.A., and Wu, J.Q. (2014). An RNA-sequencing transcriptome and splicing database of glia, neurons, and vascular cells of the cerebral cortex. J. Neurosci. *34*, 11929–11947.

Zhang, Y., and Barres, B.A. (2010). Astrocyte heterogeneity: an underappreciated topic in neurobiology. Curr. Opin. Neurobiol. *20*, 588–594.

Zuchero, J.B., and Barres, B.A. (2015). Glia in mammalian development and disease. Development *142*, 3805-3809.

Main Figures
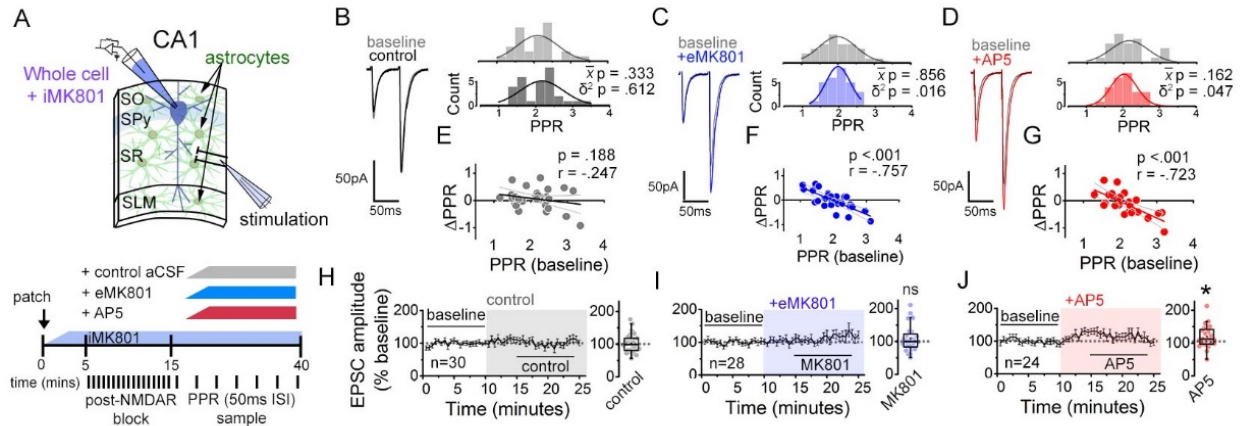
Figure 1. NMDARs contribute to synaptic strength diversity of Schaffer collateral synapses. (**A**) Experimental scheme to assess the role of non-postsynaptic NMDARs. MK801 was perfused through the patch pipette to the CA1 pyramidal neuron for 10-15 min, and pairs of stimuli (Δt = 50 ms) were applied at least 45 times at 0.1Hz to pre-block postsynaptic NMDARs prior to bath applying NMDAR antagonists (bottom). (**B-D**) Left: representative EPSC traces (average of 20 sweeps) to pairs of pulses (Δt = 50 ms) applied to Schaffer collateral axons before (baseline) and after wash-on of vehicle control (*B*), MK801 (50 µM) (*C*), or AP5 (50 µM) (*D*). Right: histograms of the PPRs recorded during the baseline and vehicle or drug application periods were fit with single Gaussian curves. The p values for the comparison of the baseline to the experimental periods for the population mean ($\bar{x}$) and variance (δ^2) were obtained by two-tailed paired sample t-test and one-tailed f-test for equal variances, respectively. (**E-G**) Scatterplots of the change in PPR vs. the initial PPR in vehicle control (*E*), MK801 (*F*), or AP5 (*G*) where ΔPPR = $PPR_{experimental}$-$PPR_{baseline}$; linear fits, Pearson's correlation coefficients (r) and p values are as indicated. X intercept: MK801 = 1.97, AP5 = 1.95. (**H-J**) Plots of normalized EPSC amplitudes before and during the application of NMDAR antagonists (shaded area); n, number of inputs examined for each experiment. Baseline and experimental periods are indicated (black bars). Right: summary bar graph. * p<0.05, Mann-Whitney U-test. Control = 30 inputs, 15 cells, 13 mice; MK801 = 28 inputs, 14 cells, 9 mice; AP5 = 24 inputs, 12 cells, 11 mice.

36
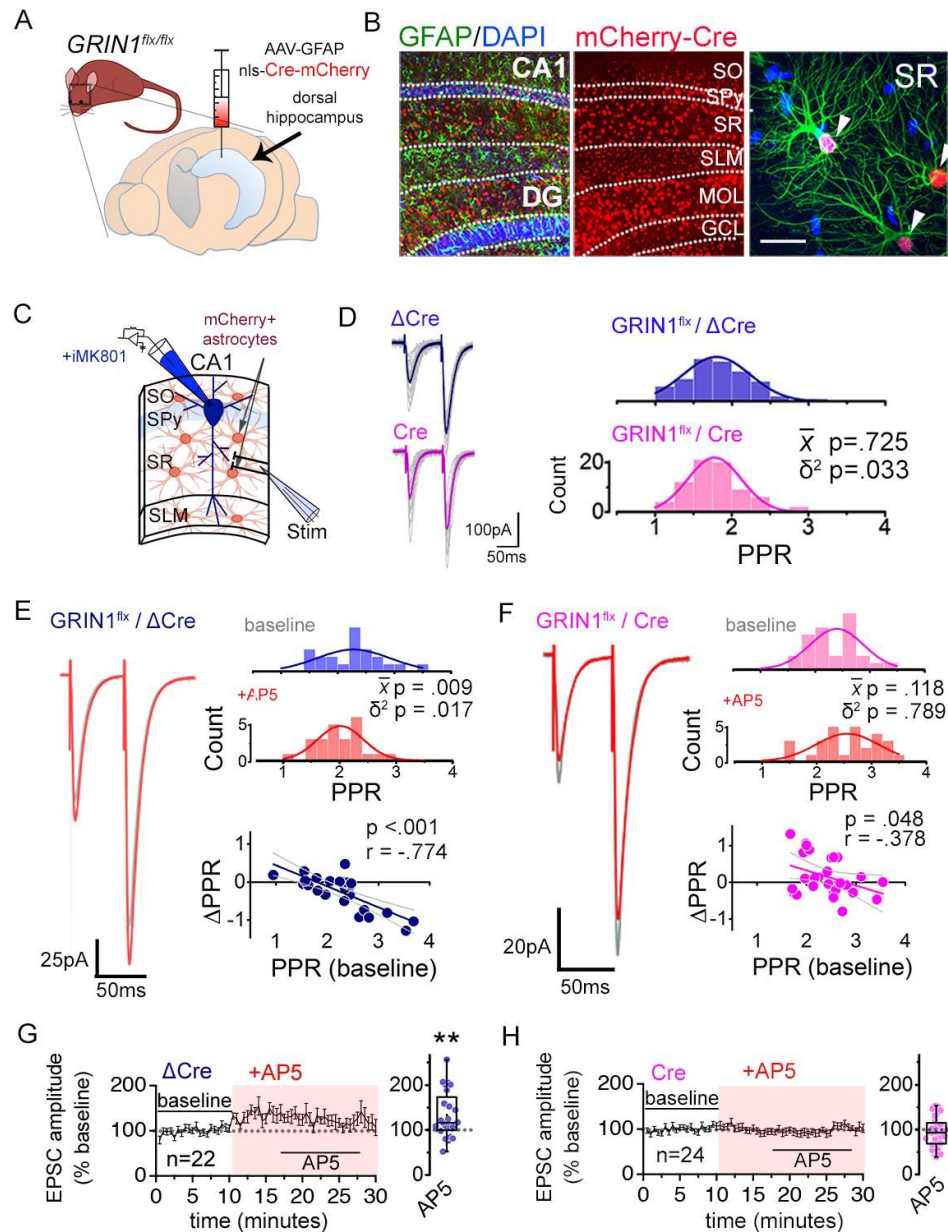
Figure 2. Astrocyte NMDARs mediate the antagonist-induced decrease in synaptic strength diversity. (**A**) Astrocyte GluN1 was conditionally knocked down by injecting AAV-GFAP104-nls-mCherry-Cre (Cre), or as a control, AAV-GFAP104-nls-mCherry (ΔCre), to the dorsal hippocampus of adult GRIN1*flx/flx* mice. (**B**) Representative image of hippocampal area CA1 immunolabelled for GFAP (green) and mCherry (red) and counterstained with DAPI (blue), 21 days after virus injection. SO, *stratum oriens*; SPy, *stratum pyramidale*; SR, *stratum radiatum*; SLM, *stratum lacunosum moleculare*; MOL, molecular layer; GCL, granule cell layer. Right: magnified view in SR showing restricted expression of mCherry to GFAP-positive astrocytes (arrowheads). Scale bar, 20 μm. (**C**) Recording scheme: CA1 pyramidal neurons were patched in acute slices prepared 21 days after ΔCre or Cre AAV infection. EPSCs were elicited by placing the stimulating electrode in the SR. Patch pipette contained MK801 for experiments in *E-H*. (**D**) Left: Averaged EPSC traces from representative recordings in slices from control ΔCre (top) or Cre (bottom) virus-infected mice. Individual traces are shown in grey. Right: Histograms of PPRs recorded from ΔCre (top) and Cre slices (bottom) were fit with single Gaussians. The p values were obtained for the population mean ($\bar{x}$) (two-tailed t-test) and variance (δ^2) (one-tailed f-test for equal variances)

comparing PPR distributions from ΔCre (n=72 inputs, 43 cells, 14 mice) and Cre (n=74 inputs, 46 cells, 12 mice) slices. (**E,F**) Left: average EPSC traces in baseline (grey) and after drug treatment (color) from a representative experiment. Right: PPR histograms (top) and ΔPPR vs. baseline PPR plots (bottom) in baseline and after bath applying AP5 (50 µM) to ΔCre (*E*) and Cre (*F*) slices. The p values for the population mean ($\bar{x}$) and variance (δ^2) are as in *D*, comparing PPRs before and after the drug treatment. Linear fits and Pearson's correlation coefficients (r) and p values are shown in scatter plots. (**G,H**) Plots of normalized EPSC amplitudes before and during the application of AP5 to ΔCre (*G*) and Cre-infected (*H*) slices (shaded area); n is the number of inputs examined. Right: summary bar graph. **p = 0.005, Mann-Whitney U-test. ΔCre +AP5 = 22 inputs, 12 cells, 5 mice; Cre +AP5 = 24 inputs, 14 cells, 5 mice.

(*Figure 2 legend continued from previous page*)

38
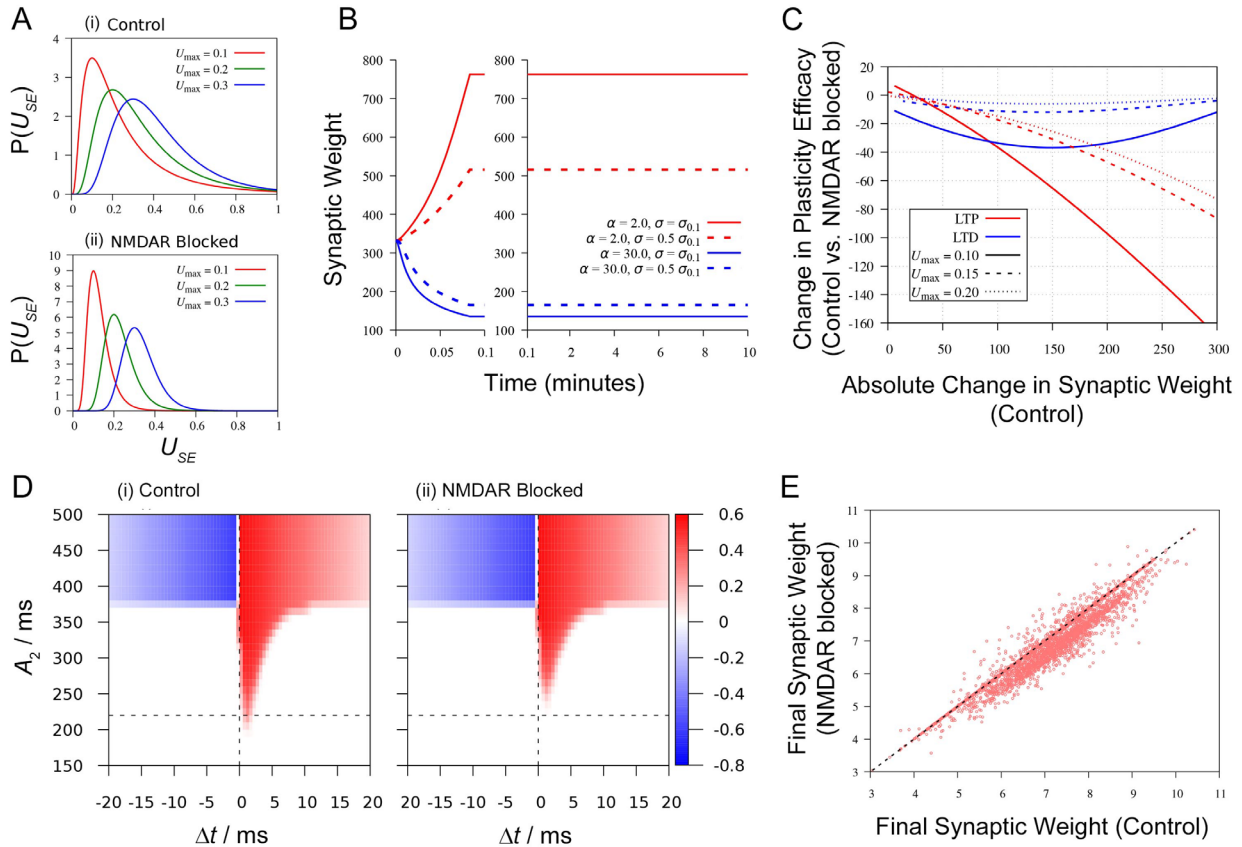
Figure 3. Synaptic strength diversity impacts long-term synaptic plasticity. (**A**) Variations of release probability distribution U_{SE}, with different peak locations (U_{max} = 0.1, red; U_{max} = 0.2, green; U_{max} = 0.3, blue) modelled using a log-normal distribution reported by Murthy et al., (1997). The plot shows release probability distributions for the control condition (i) and the condition of reduced release probability variance mimicking the NMDAR-block condition (ii). (**B**) Example results of the BCM-like learning simulation. Traces show synaptic weight function $w(t)$ for LTP (red: α = 2.0) and LTD (blue: α = 30.0) simulations where long-term synaptic plasticity is induced by applying 100 presynaptic spikes with 50 ms inter-spike intervals; the decay of synaptic plasticity has not been considered in the model. Two limiting cases of the release probability distributions of the presynaptic neuron (control, solid line; NMDAR block, dotted line; U_{max} = 0.1 for both cases) as illustrated in (*Ai*) and (*Aii*) are shown. (**C**) Plot of the difference of the synaptic weight change at w(t = 2 min) between the release probability distributions representing control and NMDAR block for LTP (red) and LTD (blue) as a function of the change in synaptic weight w(t = 2 min) for the control case over a range of potentiation or depression. The horizontal axis is defined by $w(t = 2 \text{ min}, \sigma = \sigma_{max}) - w(t = 0)$. The difference of synaptic weight in the y-axis is defined as $w\left(t = 2 \text{ min}, \sigma = \frac{\sigma_{max}}{2}\right) - w(t = 2 \text{ min}, \sigma = \sigma_{max})$ for LTP and as $w(t = 2 \text{ min}, \sigma = \sigma_{max}) - w(t = 2 \text{ min}, \sigma = \frac{\sigma_{max}}{2})$ for LTD. The relationship is shown for three different peak distributions, U_{max}, for both LTP and LTD (U_{max} = 0.1, solid line; U_{max} = 0.2, dashed line; U_{max} = 0.3, dotted line). (**D**) Simulation result using two leaky integrate-and-fire neurons. Changes in synaptic weight w(t) after giving 10 spike pairs in which the current injection to the presynaptic neuron is 500 pA and the postsynaptic neuron is A_2, in control (i) and in NMDAR blocked condition (ii). The current injection sequences to the presynaptic and the postsynaptic neurons are separated by a time difference Δt. Color intensity shows potentiation (red) and depression (blue) of synaptic weight changes. Vertical dashed line: Δt = 0. Horizontal dashed line: the least A_2 to evoke LTP under the NMDAR-block condition. (**E**) A comparison of the simulation result using Poisson spike trains. Each data point represents the synaptic weights after applying the same pair of Poisson sequences

for the release probability distribution representing the control condition (x-axis) and the NMDAR block condition (y-axis). The NMDAR block condition consistently shows smaller synaptic weight compared to the control condition.

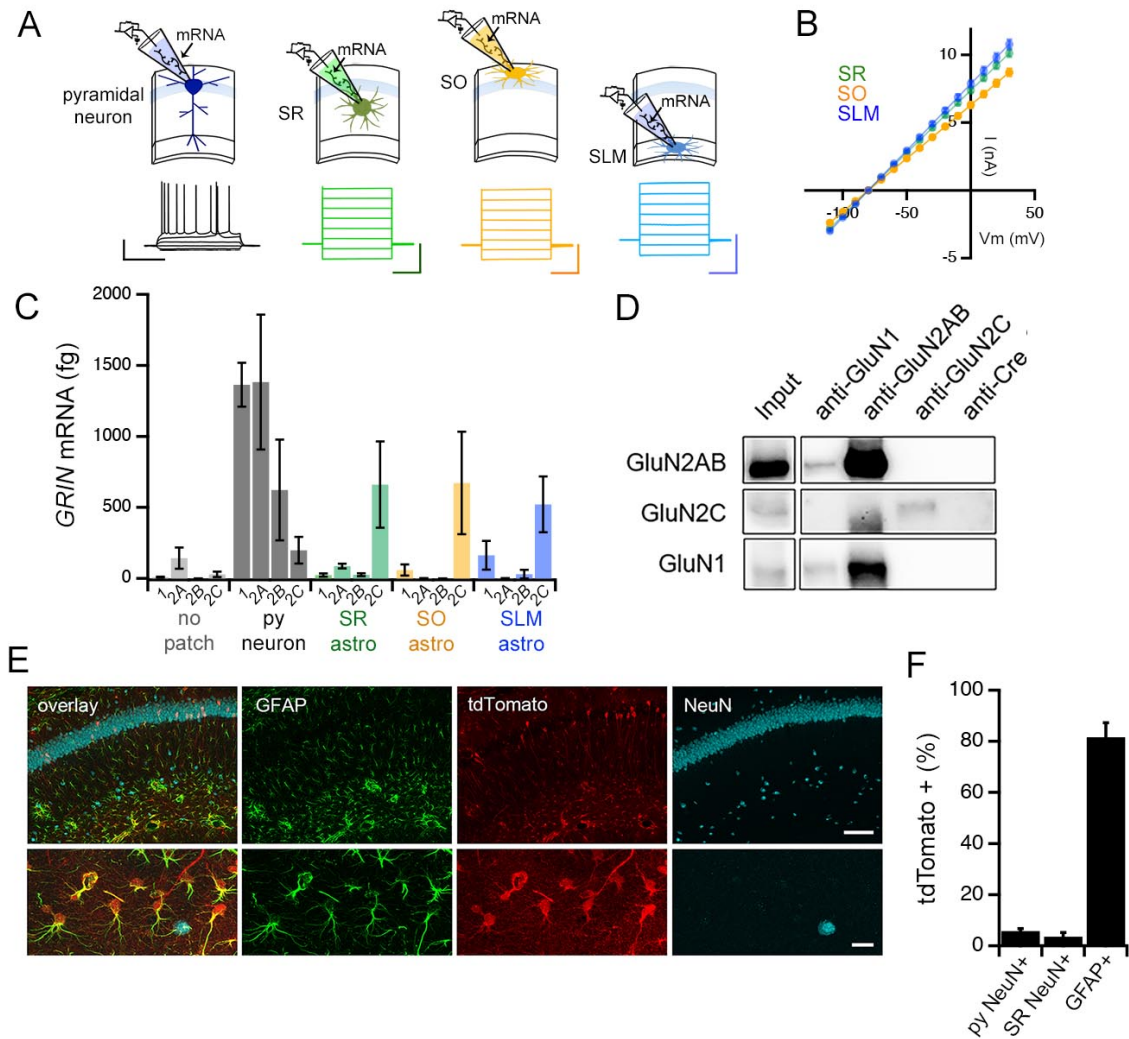(*Figure 3 legend continued from previous page*)

Figure 4. Adult mouse hippocampal astrocytes express GluN2C-NMDA receptors. (**A**) Top: patch RT-PCR strategy. Bottom: representative voltage responses to current steps in CA1 pyramidal neuron (far left, black), and current responses to voltage steps in astrocytes in *stratum radiatum* (SR, green), *stratum oriens* (SO, yellow), and *stratum lacunosum moleculare* (SLM, blue). Scale bars: neuron, 40 mV, 500 ms; astrocytes, 6 nA, 200 ms. (**B**) Summary of I-V curves of astrocytes obtained before collecting RNA. N = 39 cells, 36 slices, 9 mice for each layer. (**C**) Summary of RT-PCR analysis for mRNA encoding indicated NMDAR subunits: *GRIN1* (1), *GRIN2A* (2A), *GRIN2B* (2B), and *GRIN2C* (2C). Control samples (no patch) were obtained by inserting the electrode into the slice without patching cells. *GRIN2D* levels were undetectable in all cells examined (data not shown). (**D**) Western blots of co-immunoprecipitations performed using adult mouse hippocampal extracts with the indicated antibodies where anti-Cre antibody is used as a negative control. The blots are probed for GluN2A/2B (top row), GluN2C (middle row) or GluN1 (bottom row). (**E**) Representative brain sections of *GRIN2C*-Cre mice crossed to a tdTomato reporter line (Ai9), showing hippocampal area CA1 immunolabelled for GFAP, tdTomato and NeuN; scale bars, 160 μm (top), 25 μm (bottom). (**F**) Quantification of % cells that are positive for tdTomato amongst NeuN-labelled cells in *stratum pyramidale* (left) and SR (middle) and GFAP-labelled cells (right).
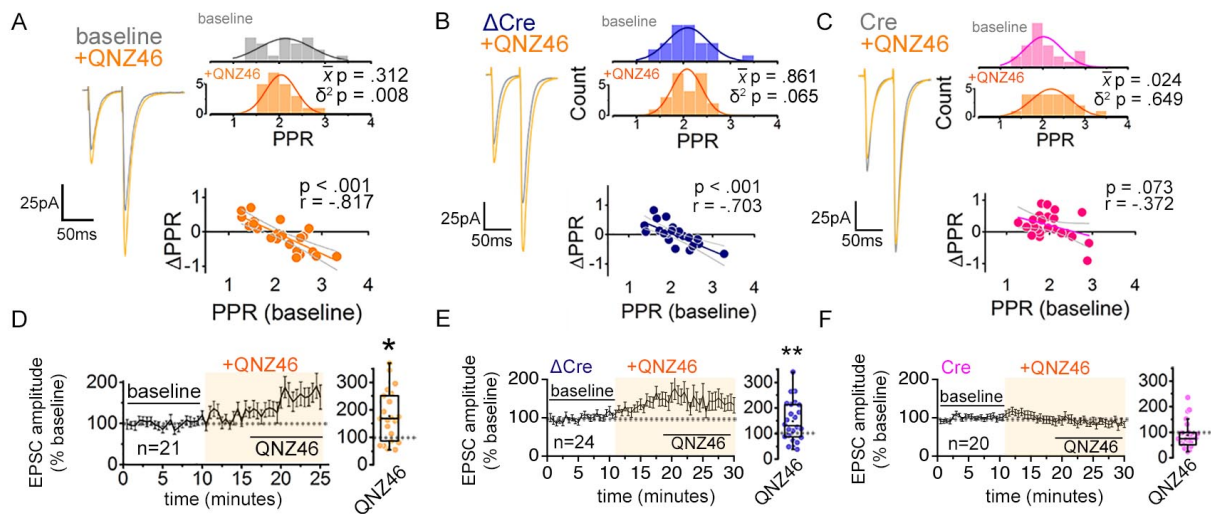
Figure 5. Inhibiting GluN2C NMDARs reduces PPR variability in a manner dependent on astrocyte expression of GluN1. (**A-C**) Left: representative EPSC traces (average of 20 sweeps) to pairs of pulses (Δt = 50 ms) applied to Schaffer collateral axons in baseline and after wash-on of QNZ46 (25 μM). Right: PPR histograms (top) and ΔPPR vs. baseline PPR plots (bottom) before and after bath applying QNZ46 to control uninfected (*A*), ΔCre (*B*) and Cre (*C*) slices. The p values were obtained for the population mean ($\bar{x}$) (paired sample t-test) and variance (δ^2) (one-tailed f-test for equal variances) comparing PPRs before and after the drug treatment. Linear fits and Pearson's correlation coefficients (r) and p values are shown in scatter plots. (**D-F**) Plots of EPSC amplitudes (normalized to the baseline average) before and during the application of QNZ46 to control uninfected (*D*), ΔCre (*E*) and Cre-infected (*F*) slices (shaded area) where n is the number of inputs examined for each experiment. Baseline and experimental periods are indicated (black bars). Box plots show the summary of normalized EPSC amplitudes during the QNZ46 application. *p<0.05, **p = 0.005, Mann-Whitney U-test was used to compare the control to the drug conditions. No virus infection +QNZ46 = 21 inputs, 11 cells, 7 mice; ΔCre +QNZ46 = 24 inputs, 12 cells, 5 mice; Cre +QNZ46 = 20 inputs, 12 cells, 6 mice.
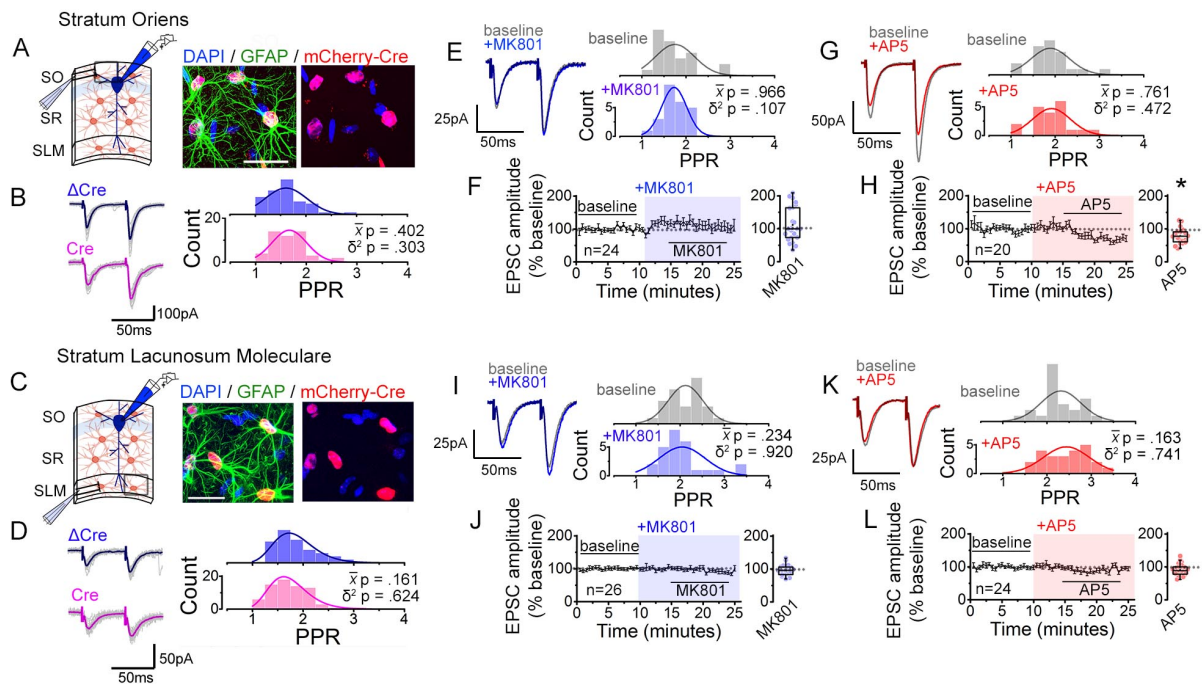
Figure 6. Interfering with astrocyte NMDARs has little effect on synaptic strength diversity in the *stratum oriens* (SO) and the *stratum lacunosum moleculare* (SLM). (**A**) Left: recording scheme. Right: confocal image from SO in CA1 showing nls-mCherry-Cre-positive astrocytes labelled with GFAP and DAPI. Scale bar, 20 μm. (**B**) Average (color) and individual (grey) EPSC sweeps from representative recordings by stimulating SO of ΔCre and Cre infected slices. PPR histograms from ΔCre (top) and Cre slices (bottom) fit with single Gaussians. [p values: comparisons of population mean ($\bar{x}$) (Mann-Whitney test) and variance (δ^2) (one-tailed f-test for equal variances) between ΔCre and Cre.] ΔCre, n = 50 inputs, 25 cells, 7 mice; Cre, n = 50 inputs, 25 cells, 7 mice. (**C,D**) Same analysis as in *A,B* for SLM. ΔCre, n = 67 inputs, 47 cells, 12 mice; Cre, n = 71 inputs, 49 cells, 12 mice. (**E,G**) Representative EPSC traces and PPR histograms of from SO stimulation in baseline and after applying MK801 (*E*) or AP5 (*G*). (**F,H**) Normalized EPSC amplitudes before and after applying MK801 (*F*) or AP5 (*H*) (shaded area) in SO. Right, summary bar graph. MK801, n = 24 inputs, 12 cells, 6 mice; AP5, n = 20 inputs, 10 cells, 7 mice. * p<0.05 Mann-Whitney U-test. (**I,K**) Same analysis as in *E,G* for PPRs elicited in SLM in control and MK801 (*I*) or AP5 (*K*). (**J,L**) Same analysis as in *F,H* with MK801 (*J*) or AP5 application (*L*). MK801: n = 26 inputs, 13 cells, 8 mice; AP5, n = 24 inputs, 12 cells, 6 mice.

43

Supplementary Figures
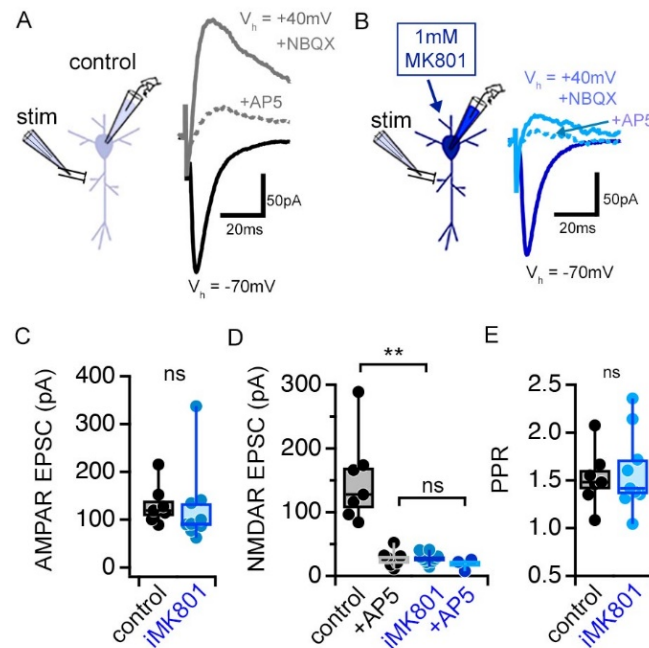
Supplementary Figure S1. MK801 (1mM) in the patch pipette (iMK801) completely blocks postsynaptic NMDARs. (**A-B**) Representative traces of EPSC recorded at a holding potential (V_h) of -70mV using control (*A*) or MK801-containing (*B*) pipette solution to measure AMPAR-mediated currents. EPSCs were recorded at a V_h of +40mV and in the presence of NBQX (10 μM) to measure isolated NMDAR-mediated currents. AP5 (20 μM) was subsequently added to the bath to confirm the NMDAR-dependence of EPSCs. EPSCs were sampled following a pre-experiment stimulation period that consisted of at least 45 pairs of pulses delivered at 0.1Hz at a V_h of -70mV. (**C**) AMPA-mediated EPSCs are no different between control and iMK801experiments. (**D**) NMDAR-mediated EPSCs are completely abolished by the presence of iMK801. (**E**) Paired pulse ratios (PPRs) measured at V_h -70mV are not altered by iMK801. Control n = 7 cells, 7 slices, 2 mice; Control +AP5 n = 7 cells, 7 slices, 2 mice; iMK801 n = 9 cells, 9 slices, 3 mice; iMK801 +AP5 n = 3 cells, 3 slices, 2 mice. ns p > .05, ** p < .0001 two-tailed t-test (*D, E*) or Mann-Whitney U test (*C*).

44
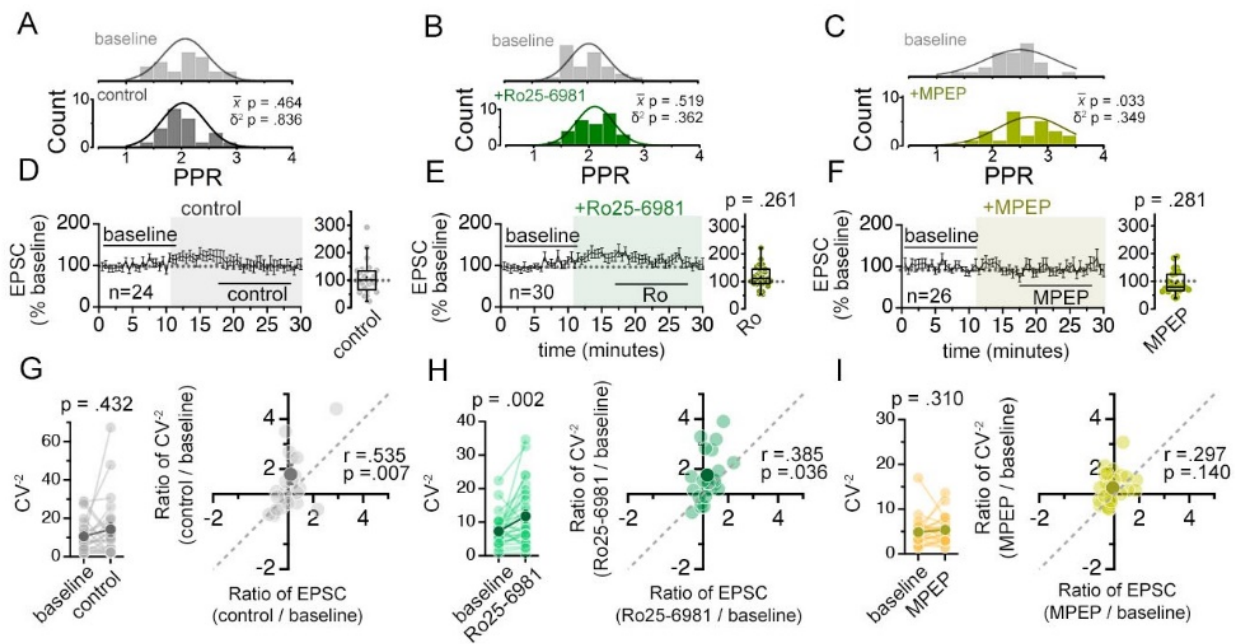
Supplementary Figure S2. Antagonists of GluN2B-containing NMDARs (Ro25-6981) or mGluR5 (MPEP) do not alter synaptic weight diversity. (**A-C**) Histograms of PPR distributions during the baseline (*top histogram*) and control aCSF or drug application (*bottom histogram*) were fit with single Gaussian curves. The p values obtained for the population mean ($\bar{x}$) (two tailed paired sample t-test for *A, B*, Wilcoxon signed rank test for *C*) and variance (δ^2) (one-tailed f-test for equal variances) comparing the baseline to the aCSF/drug application periods are shown in the graphs. (**D-F**) Plots of EPSC amplitudes (normalized to the baseline average) before and during the application of NMDAR antagonists (shaded area) where n is the number of inputs examined. Baseline and experimental periods are indicated (black bars). Box plots to the right show the summary of normalized EPSC amplitudes during the application of indicated inhibitors. P-values are the result of Mann-Whitney U tests comparing EPSC change drug application period to the corresponding period in control experiments. (**G-I**) Left: Mean (dark circles) and individual (light circles) CV^{-2} of EPSCs during the baseline and aCSF/drug application periods. P-values shown are the result of Wilcoxon signed rank tests. Right: Scatterplot of the relative change in CV^{-2} ($CV^{-2}_{experimental}/CV^{-2}_{baseline}$) against the relative change in EPSC amplitude ($EPSC_{experimental}/EPSC_{baseline}$) for the mean (dark circles) and individual inputs (light grey circles). Pearson's correlation coefficients (r) and p values are shown in the graph. Control n = 12 inputs, 24 cells, 11 mice; Ro25-6981 n = 30 inputs, 17 cells, 11 mice; MPEP n = 26 inputs, 13 cells, 5 mice.
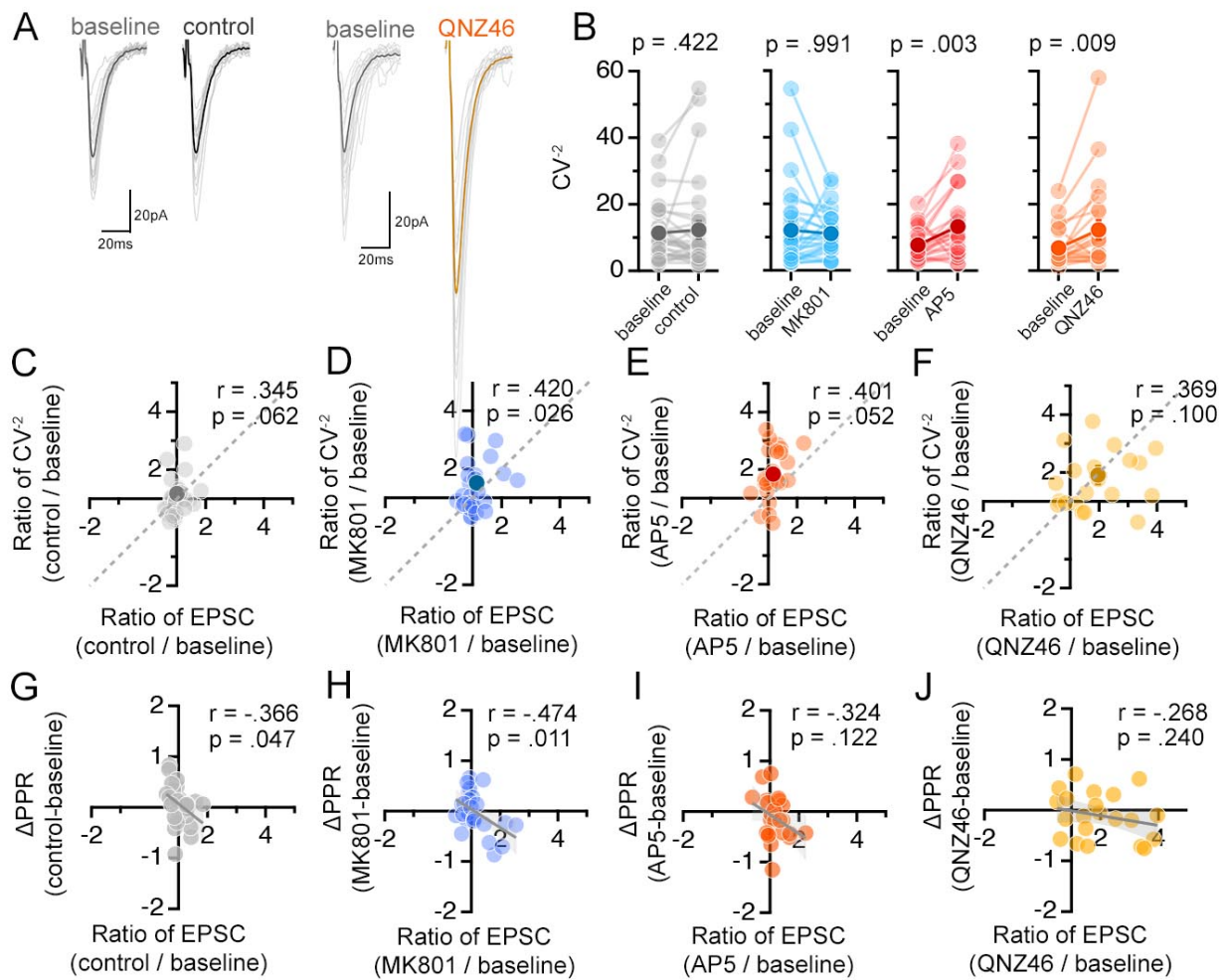
Supplementary Figure S3. NMDAR antagonists differentially influence presynaptic function. (**A**) Averaged (dark colors) and individual (light grey) EPSC traces during the baseline and experimental periods from a representative experiment. (**B**) Mean (dark circles) and individual (light grey circles) CV^{-2} of EPSCs during the baseline and aCSF/drug application periods. P-values are the result of Wilcoxon signed rank tests. (**C-F**) Scatterplot of the relative change in CV^{-2} ($CV^{-2}_{experimental}/CV^{-2}_{baseline}$) against the relative change in EPSC amplitude ($EPSC_{experimental}/EPSC_{baseline}$) for the mean (dark circles) and individual inputs (light circles). Pearson's correlation coefficients (r), p values, and the unity line (dashed) are shown in scatter plots. (**G-J**) Scatterplot of the difference in PPR ($PPR_{experimental}-PPR_{baseline}$) against the relative change in EPSC amplitude ($EPSC_{experimental}/EPSC_{baseline}$) for the mean (dark symbol) and individual inputs (light symbols). Linear fits (grey lines), Pearson's correlation coefficients (r), and p values are shown in scatter plots. Control = 30 inputs, 15 cells, 13 mice; MK801 = 28 inputs, 14 cells, 9 mice; AP5 = 24 inputs, 12 cells, 11 mice; QNZ46 = 22 inputs, 11 cells, 7 mice; Ro25-6981 n = 30 inputs, 17 cells, 11 mice; MPEP n = 26 inputs, 13 cells, 5 mice.
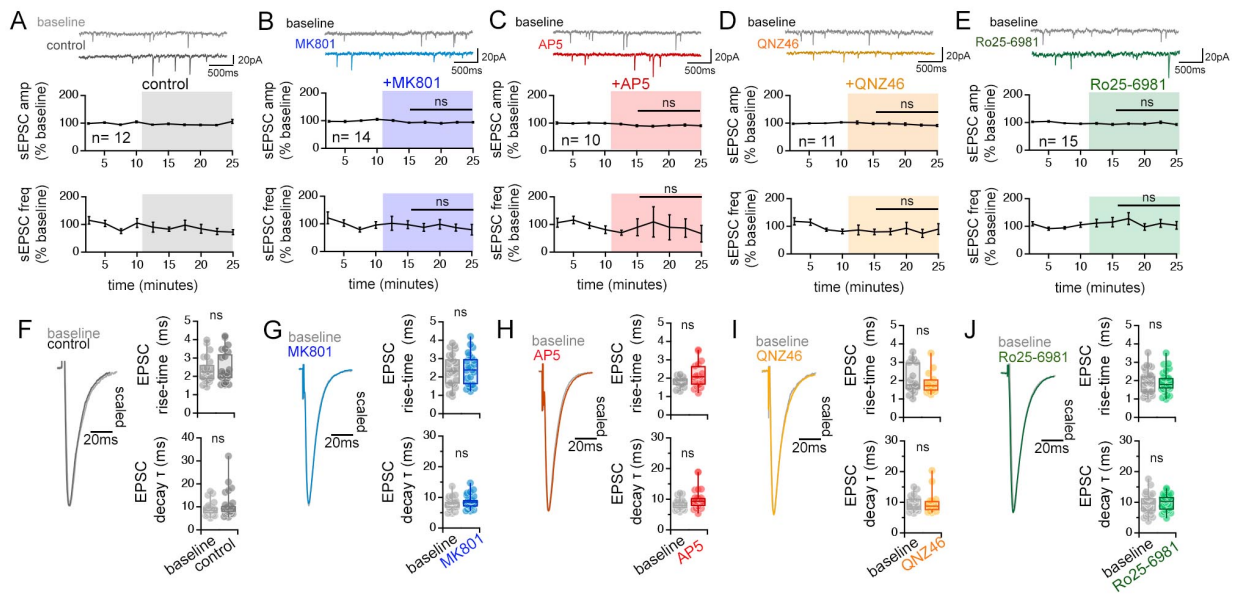
Supplementary Figure S4. NMDAR antagonists have little effect on spontaneous neurotransmission and the waveform of evoked EPSCs. (**A-E**) Representative traces and quantification of spontaneous EPSC amplitude and frequency recorded during the baseline and after applying control aCSF (*A*), MK801 (*B*), AP5 (*C*), QNZ46 (*D*), and Ro-256981 (*E*). Control n=12 cells, 10 mice; MK801 n = 14 cells, 9 mice; AP5 n = 10 cells, 9 mice; QNZ46 n = 11 cells, 8 mice; Ro25-6981 n = 15 cells, 10 mice. ns $p > .05$ one way ANOVA (amplitude), and Kruskal-Wallis ANOVA (frequency) comparing the normalized change during experimental periods across treatment conditions. (**F-J**) Left: Grand average waveforms of EPSCs recorded. Right: Box plots of EPSC risetime (top) and EPSC decay time constant (single exponential fit)(bottom) for baseline and control aCSF or drug application. ns $p > .05$ two tailed t-test or Mann-Whitney U tests. Control n = 24 inputs, 12 cells, 10 mice; MK801 n = 16 inputs, 11 cells, 11 mice; AP5 n = 26 inputs, 13 cells, 9 mice; QNZ46 n = 18 inputs, 9 cells, 6 mice; Ro25-6981 n = 32 inputs, 16 cells, 11 mice.

47
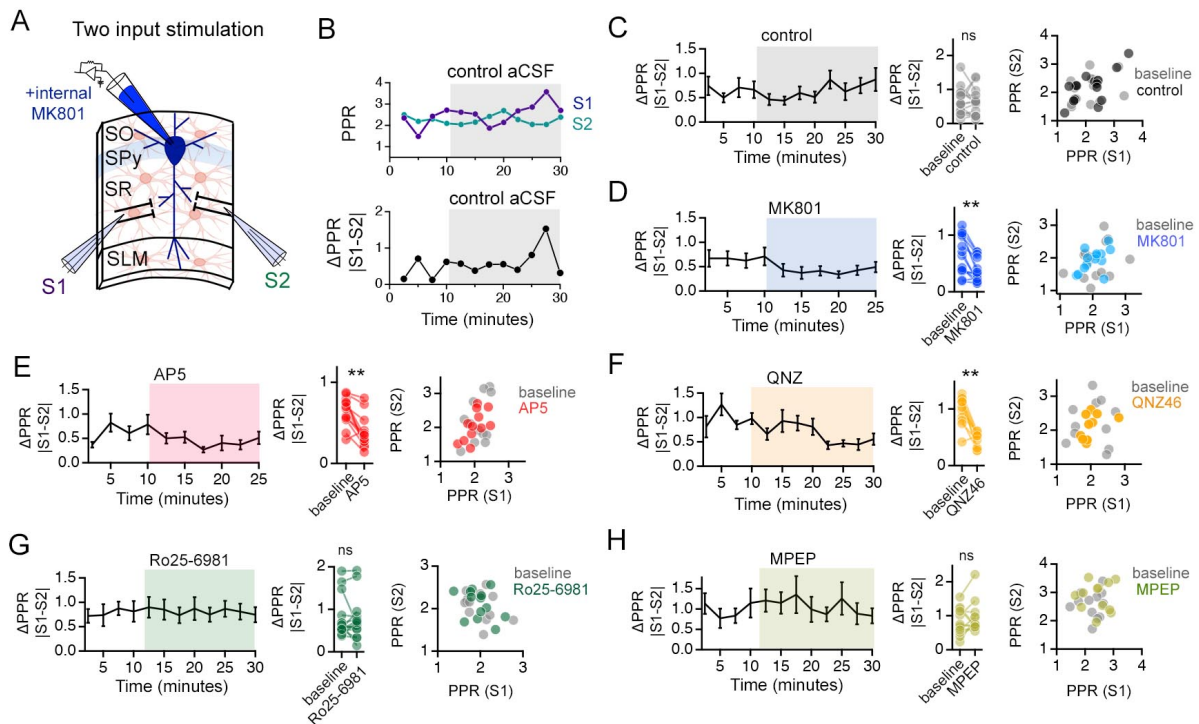
Supplementary Figure S5. NMDAR antagonists that target GluN2C-containing NMDARs reduce PPR disparity in the *stratum radiatum* (SR). (**A**) Illustration of the two-input stimulation configuration. Two independent inputs in the SR were sampled with interleaved stimulation. (**B**) The absolute difference between the PPRs of the two inputs sampled during a 2.5 min window (average of 5 sweeps) is referred to as ΔPPR ($|PPR_{S1}-PPR_{S2}|$) and is taken as a measure of variability of presynaptic strength. (**C-H**) Left: Time course of ΔPPR before and after application of antagonists. Middle: Summary plots of individual experiments comparing ΔPPR in baseline and during antagonist treatment. Right: Scatter plots comparing PPR of the two independent inputs normalized to the first EPSC amplitude for baseline and in the presence of the antagonists. ΔPPR is reduced by MK801 (*D*), AP5 (*E*), QNZ46 (*F*), but not by Ro25-6981 (*G*) or MPEP (*H*). Similarly, the scatterplots demonstrate distribution of average PPR values across pairs of inputs (S1 and S2) of PPRs by MK801, AP5 and QNZ46, all of which target GluN2C-containing NMDARs, but not by Ro25-6981 or MPEP that target GluN2B-NMDAR or mGluR5, respectively. ns $p > .05$, ** $p < .01$ Wilcoxon signed ranks test comparing baseline to drug application period. Control n = 15 pairs of inputs, 15 cells, 13 mice; MK801 n = 14 pairs of inputs, 14 cells, 9 mice; AP5 n = 12 pairs of inputs, 12 cells, 11 mice; QNZ46 n = 11 pairs of inputs, 11 cells, 7 mice; Ro25-6981 n = 15 pairs of inputs, 15 cells, 11 mice; MPEP n = 13 pairs of inputs, 13 cells, 5 mice.

48
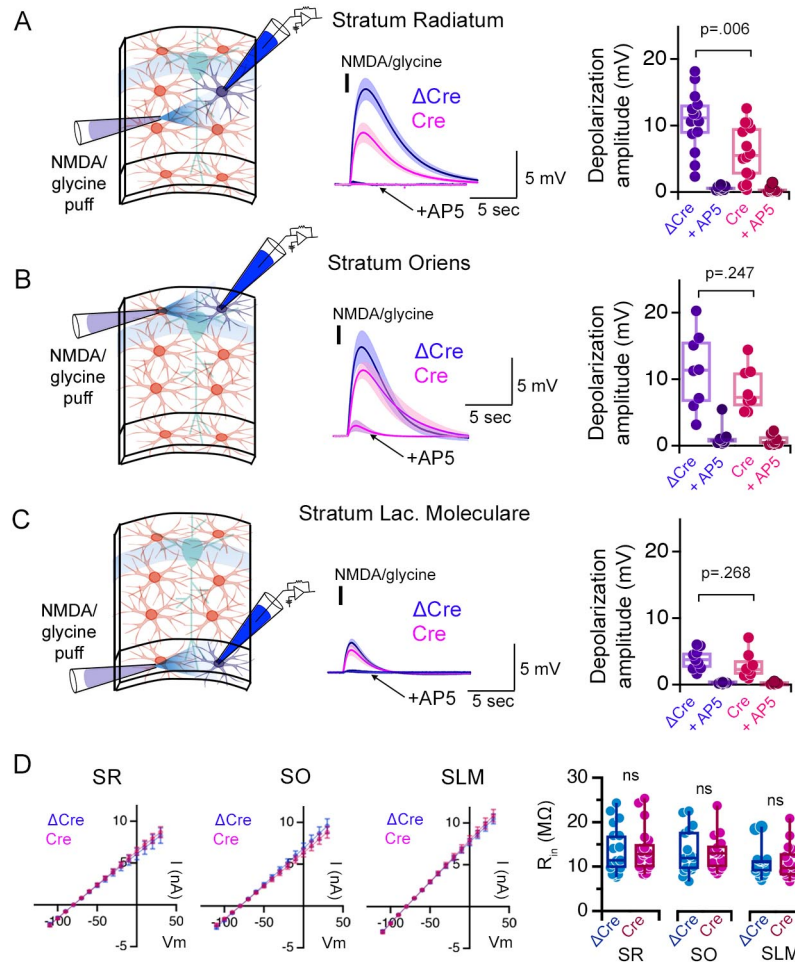
Supplementary Figure S6. Puff application of NMDA and glycine triggers the depolarization of astrocytes in hippocampal CA1 in acute slices. (**A**) Left: experimental setup. Middle: Local puff application (100 ms, black bar) of NMDA and glycine (1mM each) to astrocytes that are whole-cell patch clamped in the *stratum radiatum* (SR) elicits slow membrane depolarization (ΔCre, blue), which is prevented in the presence of AP5 (arrow). Once the depolarization is triggered, not only NMDARs but also other voltage-gated channels such as L-type calcium channels contribute to the slow depolarization (Letellier et al., 2016). The depolarization is substantially reduced when the same experiment is carried from Cre-expressing astrocytes as monitored by mCherry expression in slices infected with the AAV-GFAP104-nls-mCherry-Cre virus to knock-down astrocyte NMDARs in GRIN1 floxed mice (Cre, red). Right: Summary plot of the peak membrane depolarization in control virus infected (ΔCre) or NMDAR knock-down (Cre) slices in control aCSF or the presence of AP5. (**B-C**) Same as (*A*) except NMDA and glycine puff was applied to astrocytes patch-clamped in the *stratum oriens* (SO)(*B*) and *stratum lacunosum moleculare* (SLM)(*C*). NMDA/glycine puff-mediated depolarizations elicited in SO and SLM astrocytes are not sensitive to astrocyte NMDAR knockout. SR ΔCre n = 14 cells, 3 mice; SR Cre n = 14 cells, 3 mice. SO ΔCre n = 8 cells, 3 mice; SO Cre n = 8 cells, 3 mice. SLM ΔCre n = 9 cells, 2 mice; SLM Cre n = 8 cells, 2 mice. (**D**) Cre expression does not alter the input resistance (R_{in}) of astrocytes in any layer. IV relationships of ΔCre and Cre positive astrocytes in the SR, SO, and SLM to square voltage steps (left; 500ms duration) and quantification of R_{in} (right). SR ΔCre n = 17 cells, 8 mice; SR Cre n = 20 cells, 10 mice. SO ΔCre n = 16 cells, 10 mice; SO Cre n = 16 cells, 11 mice. SLM ΔCre n = 19 cells, 8 mice; SLM Cre n = 18 cells, 9 mice. ns p > .05, P values shown are the result of two-tailed t-tests or Mann-Whitney U tests.

49
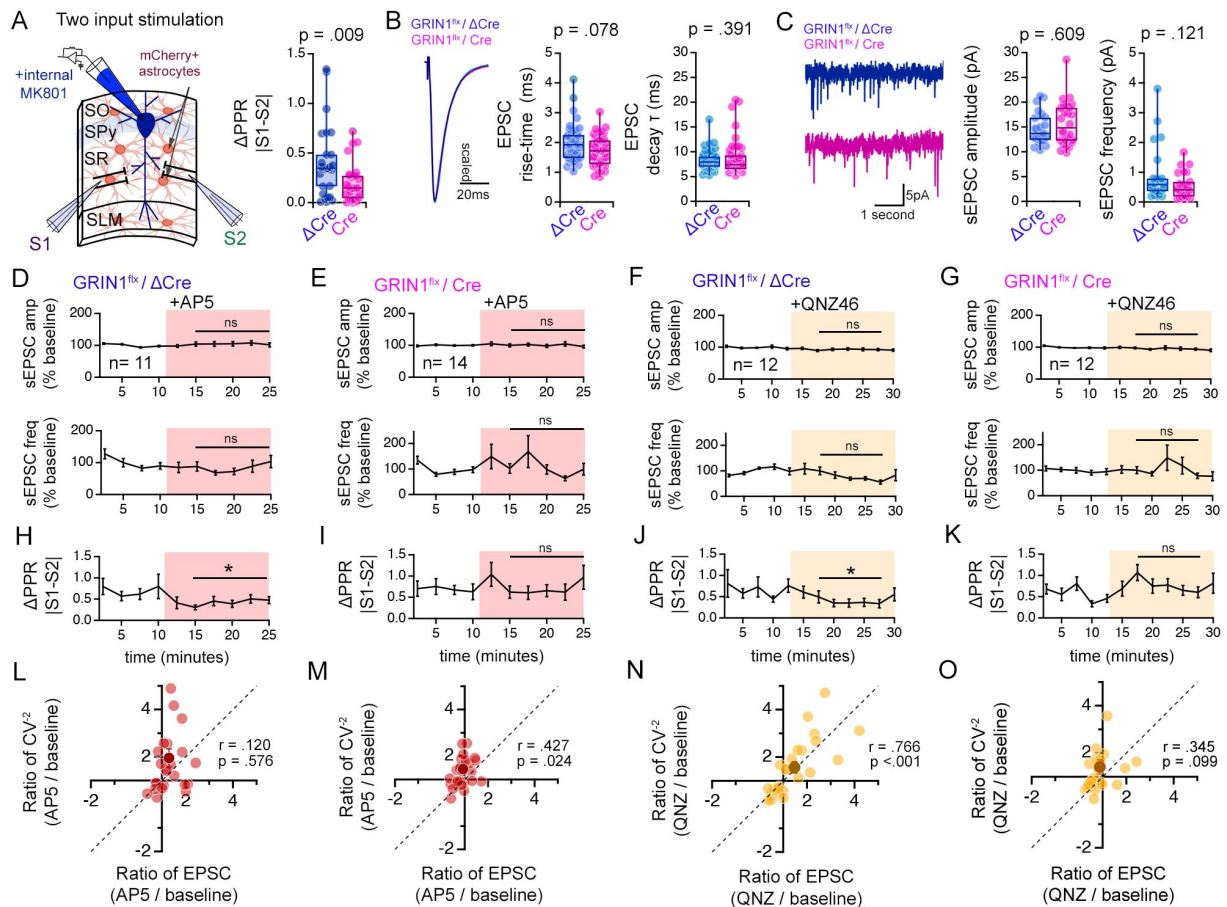
Supplementary Figure S7. Knock-down of GluN1 in hippocampal astrocytes selectively alters the PPR disparity without affecting the basic properties of synaptic transmission. (**A**) Left: Illustration of the experimental configuration of two-pathway stimulation approach to estimate PPR disparity in slices from GRIN1$^{flx/flx}$ mice infected with ΔCre or Cre virus. Right: Comparison of ΔPPR ($|PPR_{S1}-PPR_{S2}|$) between control ΔCre or Cre slices. PPR disparity (ΔPPR) is reduced in Cre infected slices compared to controls. p = .009, Mann-Whitney U test. ΔCre n = 29 pairs of inputs, 29 cells, 8 mice. Cre n = 28 pairs of inputs, 28 cells, 6 mice. (**B**) Left: Grand average waveforms of EPSCs recorded. Right: Box plots of EPSC risetime and EPSC decay time constant (single exponential fit). Each data point represents the average waveform of at least 5 sweeps of EPSCs. ΔCre n = 46 inputs, 23 cells, 8 mice. Cre n = 41 inputs, 21 cells, 6 mice. (**C**) Left: Representative traces of spontaneous EPSC (sEPSC) recordings from control ΔCre (blue) or Cre (red) slices. Right: Boxplots of sEPSC amplitude and frequency measured in ΔCre or Cre-infected slices. P values shown are the result of Mann-Whitney U test. ΔCre n = 23 cells, 5 mice. Cre n = 26 cells, 5 mice. (**D-G**) Normalized sEPSC amplitude (top) and frequency (bottom) during baseline and in the presence of AP5 or QNZ46 in control ΔCre or Cre-infected slices. Neither sEPSC amplitude nor frequency is not affected by AP5 or QNZ46. Two tailed t-test or Mann-Whitney U test, comparisons made between ΔCre vs. Cre normalized values in post drug period indicated. (**H-K**) ΔPPR ($|PPR_{S1}-PPR_{S2}|$) measurements during baseline and in the presence of AP5 or QNZ46 in control ΔCre or Cre-infected slices. The decrease in PPR disparity triggered by AP5 (*H*) and QNZ46 (*J*) is prevented upon knock-down of astrocyte NMDARs. * p < .05 Wilcoxon signed ranks test. ΔCre + AP5 n = 12 pairs of inputs, 12 cells, 6 mice. Cre + AP5 n = 14 pairs of inputs, 14 cells, 5 mice. ΔCre + QNZ46 n = 12 pairs of inputs, 12 cells, 5 mice. Cre + QNZ46 n = 12 pairs of inputs, 12 cells, 6 mice. (**L-O**) Scatterplot of the relative change of CV^{-2} (CV^{-2} $_{experimental}$/CV^{-2}$_{baseline}$) against the relative change in

50

EPSC amplitude (EPSC $_{experimental}$/EPSC$_{baseline}$) for the mean (dark symbol) and individual inputs (light symbols). Dashed lines show positive unity line. Pearson's correlation coefficients (r) and p values are shown in scatter plots. N values are the same as *H-K*.

(*Supplementary Figure S7 legend continued from previous page*)
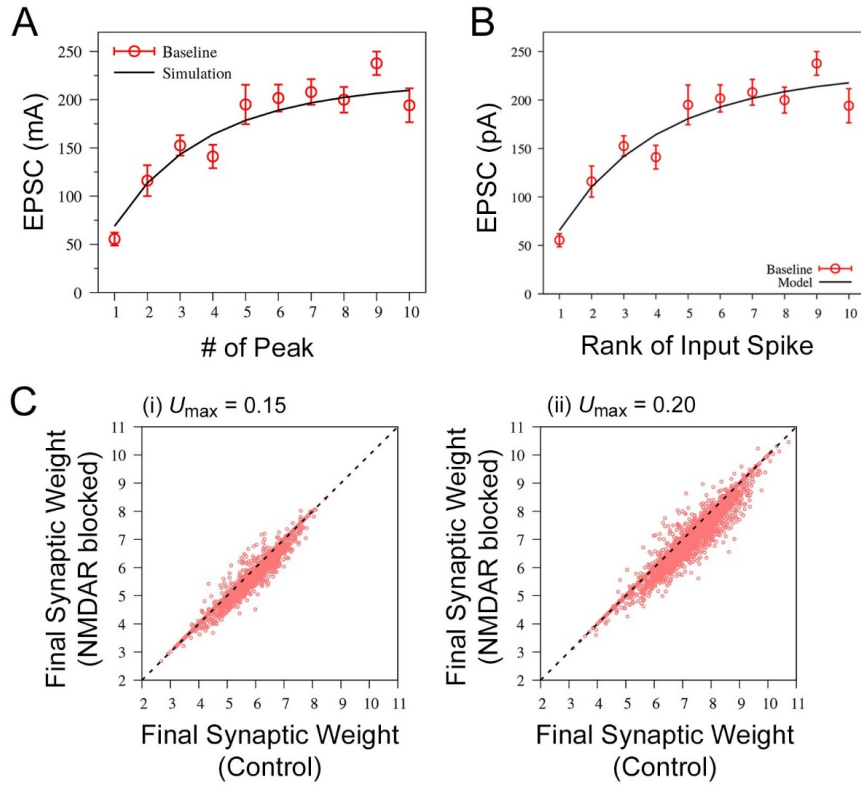
Supplementary Figure S8. Additional data for mathematical modelling experiments exploring the impact of presynaptic release probability variance on synaptic plasticity. (**A,B**) The best-fits to the experimentally obtained peak EPSC amplitudes of responses triggered by a 20Hz spike train in the BCM-like model (A) and the spiking neuron model (B). The best-fit parameters are τ_f = 540 ms, τ_{rec} = 20 ms, U_{max} = 0.1 and $w(0)$ = 332 in (A), and τ_f = 980 ms, τ_{rec} = 25 ms, U_{max} = 0.1 and $w(0)$ = 6.7 in (B). (**C**) A comparison of the synaptic weight changes observed in response to Poisson spike trains in control condition versus the NMDAR-blocked condition (reduced presynaptic release probability variance) for simulations at (i) U_{max} = 0.15 and (ii) U_{max} = 0.20. Final synaptic weight above the initial synaptic weight value of $w(0)$ = 6.7, is considered potentiation and below $w(0)$ = 6.7 is considered depression.
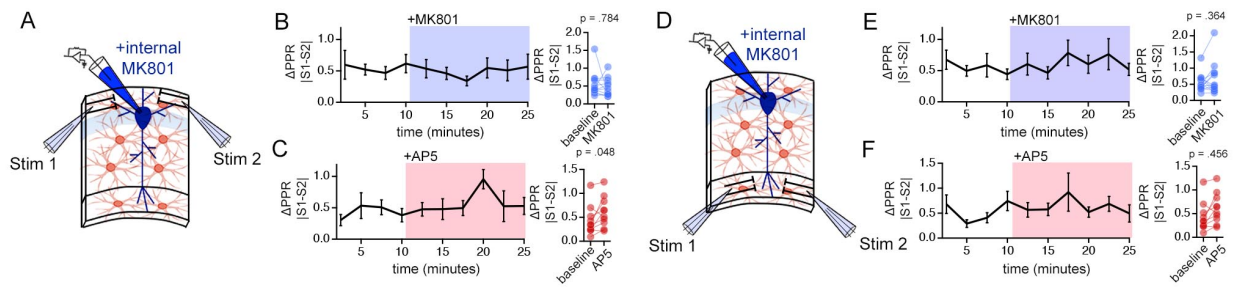
Supplementary Figure S9. MK801 and AP5 do not alter PPR disparity in the *stratum oriens* (SO) or the *stratum lacunosum moleculare* (SLM). (**A**) Illustration of the two-input stimulation configuration in SO. (**B,C**) Left: PPR disparity [ΔPPR ($|PPR_{S1}-PPR_{S2}|$)] during baseline and in the presence of MK801 (*B*) or AP5 (*C*). Right: Summary plot of ΔPPR. Neither MK801 nor AP5 application influences the PPR disparity. (**D-F**) Same experiments as described for (*A-C*) carried out in SLM. Similarly to SO recordings, MK801 and AP5 have no effects of PPR disparity in SLM. P-values are the result of Wilcoxon signed rank tests. SO MK801 n = 12 pairs of inputs, 12 cells, 6 mice; SO AP5 n = 10 pairs of inputs, 10 cells, 7 mice; SLM MK801 n = 13 pairs of inputs, 13 cells, 8 mice; SLM AP5 n = 12 pairs of inputs, 12 cells, 6 mice.